Master's Degree Dissertation

Master's Degree in Industrial Engineering

Design and Simulation of a Microgrid used in a More Electric Aircraft

Project Report

Author:	Jordi Montmany Cardó
Supervisors:	Sheng Wang and Wenlong Ming
Lecturer:	Daniel Montesinos Miracle
Date:	September 2022

ETSEIB

Escola Tècnica Superior
d'Enginyeria Industrial de Barcelona

UPC

ETSEIB

Abstract

Electric mobility plays a crucial role in energy transition. Nowadays, full electric cars are already a reality, but it is not the same for aircrafts. Moving towards electric aircraft implies numerous benefits in terms of greenhouse gas emissions, cost savings, maintenance, noise pollution and safety. More electric aircraft (MEA) is the next step between traditional and full electric aircraft. In a MEA, almost all the pneumatic and hydraulic actuators have been replaced by electric drives. Due to this fact, aircraft power systems are becoming more complex, hence the importance of protections and a control strategy. That is why power electronics are essential in this new era of transportation.

This project consists in the design and simulation of an aircraft microgrid including its generators, power converters, loads and protections. The microgrid architecture is based on a variable frequency distribution topology used by commercial planes such as Boeing 787.

In the literature review chapter, some aspects regarding the state of the art are discussed such as power generation and distribution strategies, MEA characteristics or weight reduction.

A lot of research is being done with DC power distribution systems for aircrafts. Basically, because it is the lightest power architecture topology. An important chapter of this dissertation addresses the design and simulation of a solid-state circuit breaker. It is an innovative design that has not yet been published.

The simulation has been done using Simulink. It has been useful to show the interactions between the components of the microgrid and its way of operating. Some characteristics such as harmonics, rated values and voltage and current ripples have been checked using DO-160G industrial aircraft standard.

The results have shown that essential parameters meet the standards required by DO160-G under normal operation. It has been demonstrated that the system can extinguish and isolate different faults in more than acceptable times.

ETSEIB

Table of contents

ETSEIB

Abbreviation

- **MEA** More electric aircraft.
- **AEA** All Electric Aircraft
- **EPA** Electric propelled Aircraft
- **VSVF** Variable Speed Variable Frequency
- **VSCF** Variable Speed Constant Frequency
- **CSCF** Constant Speed Constant Frequency
- **APU** Auxiliary Power Unit
- **ATRU** Auto Transformer Rectifier Unit
- **ATU** Auto Transformer Unit
- **CB** Circuit Breaker
- **CSD** Constant Speed Drive
- **DS** Distribution System
- **ECS** Environmental Control System
- **EMC** Electromagnetic Compatibility
- **EMI** Electromagnetic Interference
- **EMS** Energy Management System
- **EPDS** Electric Power Distribution System
- **EPS** Electric Power System
- **GPU** Ground Power Unit
- **AC** Alternate Current
- **DC** Direct Current

1. Preface

1.1. Origin of the project and motivation

Nowadays, traditional airplanes are increasing their electrification level turning into More Electric Aircrafts (MEA). This trend presents numerous advantages such as security, energy efficiency, flexibility in power generation and distribution, greenhouse gas emissions and noise reduction. Reliability can be improved as well because of the possibility of faster failure isolation. By increasing the number of electronic components and electric drives, the aircraft power system becomes more complex. Thus, it is necessary to build a simulation platform to study as many adverse cases as possible and assess the system response.

The first motivation point of this project is an economic aspect. As explained above, an aircraft power system is such a complex system to build, hence it is high-priced. Before building anything, it is fundamental to design and simulate the aircraft microgrid. A simulation platform helps to develop and test the microgrid, therefore a lot of money is saved.

The second point is an ecological aspect. Environmental impact is a critical issue in aeronautics due to greenhouse gas emissions. One kilogram of mass saving in each flight could result, approximately 1700 tons of fuel saving and a reduction of 5400 tons of CO_2 emissions per year for all air traffic [17]. Therefore, it is important to move towards the lightest microgrid in order to reduce CO_2 emissions.

1.2. Requirements

To move forward with the project, it is necessary to review the literature to check how the start of the art is. Aspects such as power architecture (generation and distribution), power converters and protection systems must be analysed.

Industrial standards research for aircraft microgrids has been done to build the simulation with real values used in aircraft industry. The standard used is the DO-160G and it contains the limits for rated values, ripples and harmonic distortion.

ETSEIB

2. Introduction

2.1. Project objectives

The main objective of this project is to design and simulate an aircraft microgrid in order to study and improve its electrical characteristics. Some aspects that have to be chosen and designed are power converters, power architecture, component selection and protection strategy. Another side objective is to compare different power architecture topologies to find the most efficient one since not every case can be simulated. The last objective is to design and simulate both AC and DC protections that suit the aircraft microgrid.

2.2. Project scope

This project scope goes from the literature review of power electronics in MEA to the microgrid simulation with Simulink passing through the design stage. The main tasks to develop are:

- Literature review of power electronics and power architectures in MEA
- Literature review of control and protection of aircraft microgrids
- Study and mathematical modelling of power electronics principles
- Design a MEA microgrid based on a variable frequency power architecture
- Simulation study on MEA microgrid and power electronics system using Simulink

3.   Literature review and state of the art

3.1. Traditional aircraft vs MEA

In a traditional aircraft, jet engine is in charge to produce thrust and to power hydraulic, pneumatic and electrical systems. Furthermore, it drives gearbox mounted units such as fuel, oil and hydraulic pumps. Flight control actuators use hydraulic power while pneumatic power is used for pressurization and cooling of the cabin, engines starting and for de-icing the wings. Electric generator supplies all the electrical loads such as computers and avionics systems (see figure 1).
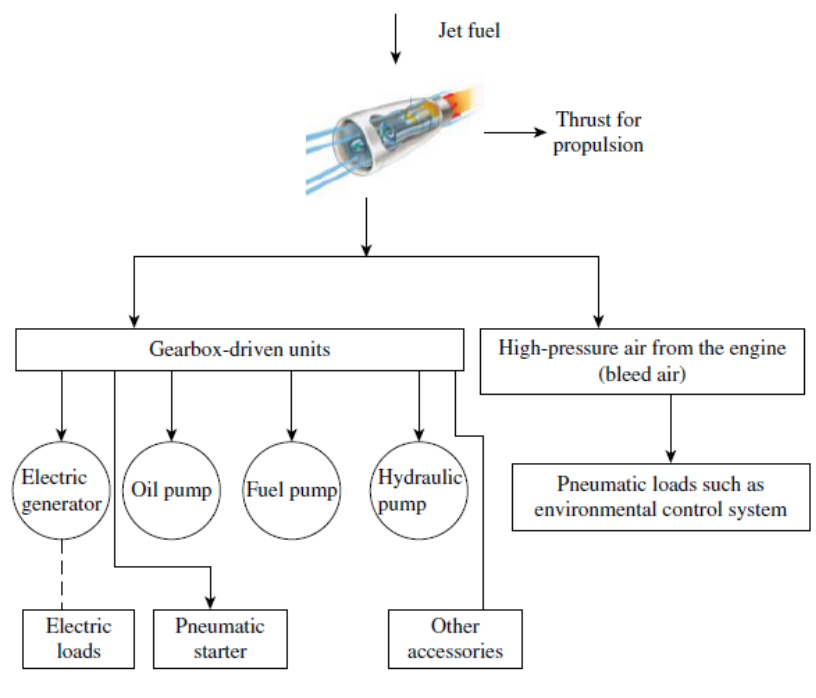

Fig. 1   Traditional aircraft power scheme
Source: [14]

However, in a More Electric Aircraft, almost all the traditional aircraft loads have turned into electrical ones, including de-icing system, environmental control systems (ECSs) and pumps. The motor used to produce thrust is attached to an electric generator (figure 2).
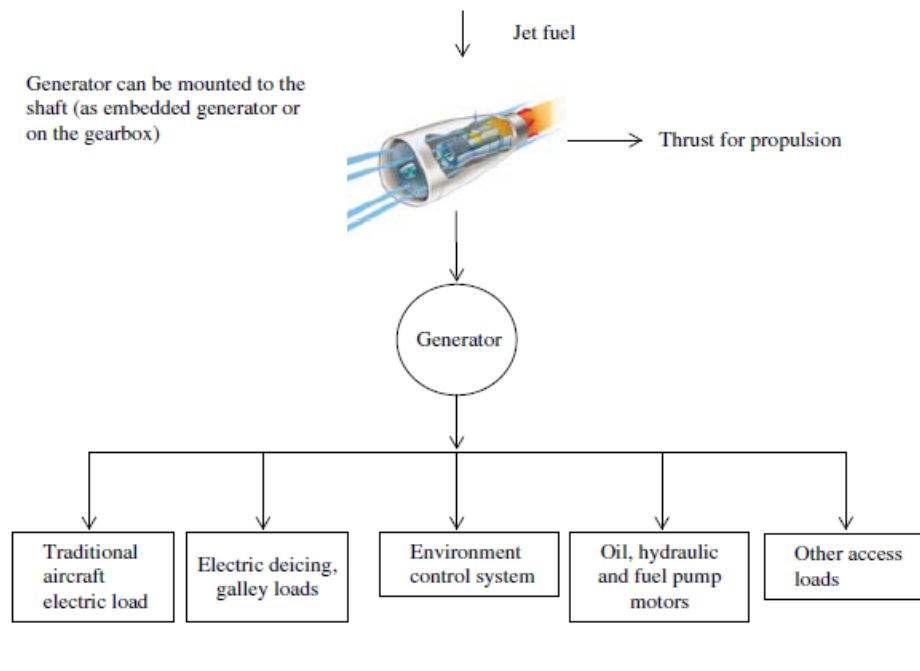
ETSEIB

Fig. 2   MEA power scheme
Source: [14]

3.2. MEA benefits

Main benefits of a MEA system are listed and discussed below [18, 19]:

• Possibility to design a major number of sophisticated systems to improve the flight comfort since more electric power is used.

• Easy monitoring of electrical systems enhances maintenance and reliability. Also, predictive maintenance is easier to implement because the performance trend can be better observed.

• Overall engine performance is improved due to reduction or elimination of bleed air. In traditional aircrafts, this air is used to start the motors, pressurize toilet water, anti-icing of motor and wings, pressurize the cabin, air conditioning, pressurize hydraulic system and so on. Bleed air decreases the motor power, degrades its performance and consumes more fuel, hence pneumatic systems are replaced by electric systems. The summarized benefits regarding elimination of bleed air are:

- Increased overall performance
- Elimination of flammable fluids and hight-temperature ducts
- Reduced maintenance and ground support

• Possibility to remove the engine accessory gearbox because it is not necessary to generate constant frequency voltage.

3.3. MEA architecture. Power generation

Three types of power generation are used in aircrafts: Constant Speed Constant Frequency (CSCF), Variable Speed Variable Frequency (VSCF), Variable Speed Variable Frequency (VSVF) and DC. They are described below.

3.3.1. Constant Speed Constant Frequency (CSCF)

It uses a Constant Speed Drive (CSD) connected between the engine and the generator to keep the mechanical speed constant. Thus, frequency is constant too. In the example below (figure 3), the generation system powers a three-phase 115 VAC / 400 Hz bus.
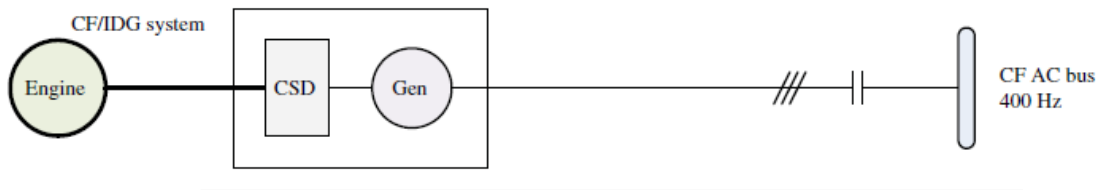
Fig. 3   CSCF power generation scheme
Source: [14]

3.3.2. Variable Speed Constant Frequency (VSCF)

They use an AC/AC converter or a cycloconverter after the generator to make the frequency constant instead of a CSD. The top strategy in figure 4 uses a cycloconverter to transform variable frequency to constant frequency. The second system uses an AC/AC converter, which is also an AC/AC converter but with an intermediate DC link.

ETSEIB
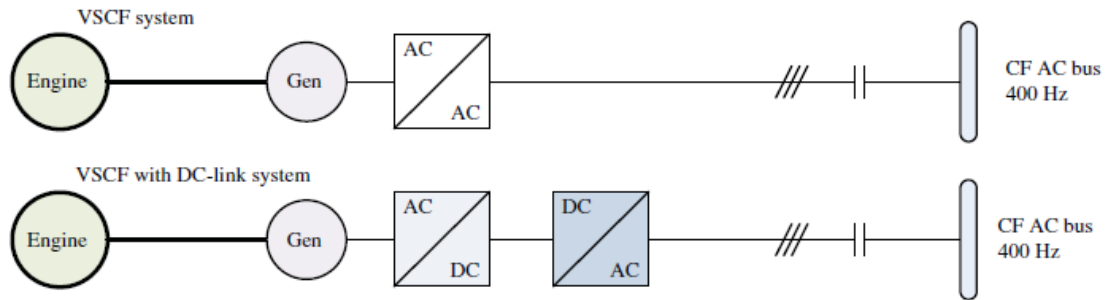
Fig. 4   VSCF power generation scheme
Source: [14]

3.3.3.   Variable Speed Variable Frequency (VSVF)

There is nothing between the main engine and the generator. The bus frequency changes proportionally to the engine speed. It can vary between 360 Hz and 760 Hz. As seen in figure 5, generator powers directly a 115 VAC or 230 VAC variable frequency bus.

Fig. 5   VSVF power generation scheme
Source: [14]

3.3.4.   DC

A rectifier is connected after the generator to convert AC to DC power. Three voltage levels are mainly used: 270 VDC, ±270 VDC and 28 VDC. The first scheme consists of a variable frequency generation at 115 VAC an then it is converted to 270 VDC using a rectifier. The second example generates 28 VDC for emergency cases. It uses a permanent magnet generator (figure 6).

ETSEIB
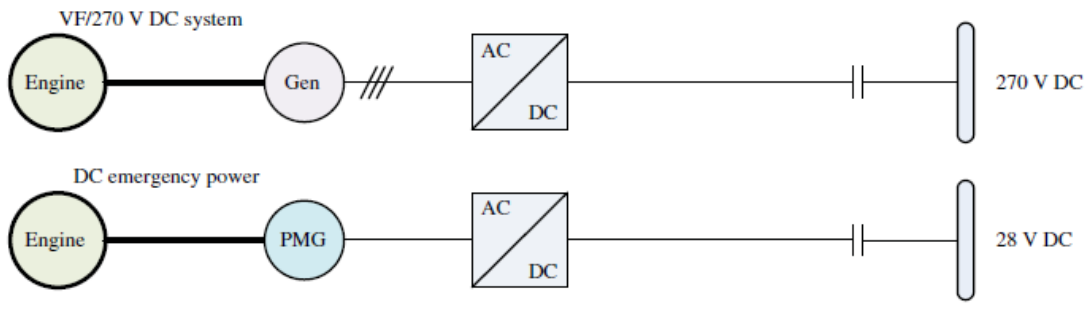
Fig. 6   DC power generation scheme
Source: [14]

3.4. Power distribution

The typical MEA power distribution architectures depending on the main bus type are the following [20]:

1) Constant frequency distribution. Normally 115 VAC/ 400 Hz

2) Variable frequency distribution (low and high voltage)

2.1) 115 VA / 360 – 800 Hz / 270 VDC

2.2) 230 VAC / 360 – 800 Hz / ±270 VDC

3) DC distribution. Normally ±270 VDC

3.4.1.   Constant frequency distribution

This architecture has been widely used in commercial aircrafts since its development in the 1960s. A320 and B737 are based on this architecture.

 It uses a constant speed drive (CSD) to convert the variable speed of the engine shaft to constant speed upstream the generator. Thus, the frequency is constant.

A transformer rectifier unit is used to convert the AC power to 28 VDC to feed the avionics and other low power loads. However, AC loads are powered directly from the AC bus. In every architecture, there is also a battery-inverter set to power the AC bus in case of emergency (figure 7).

ETSEIB
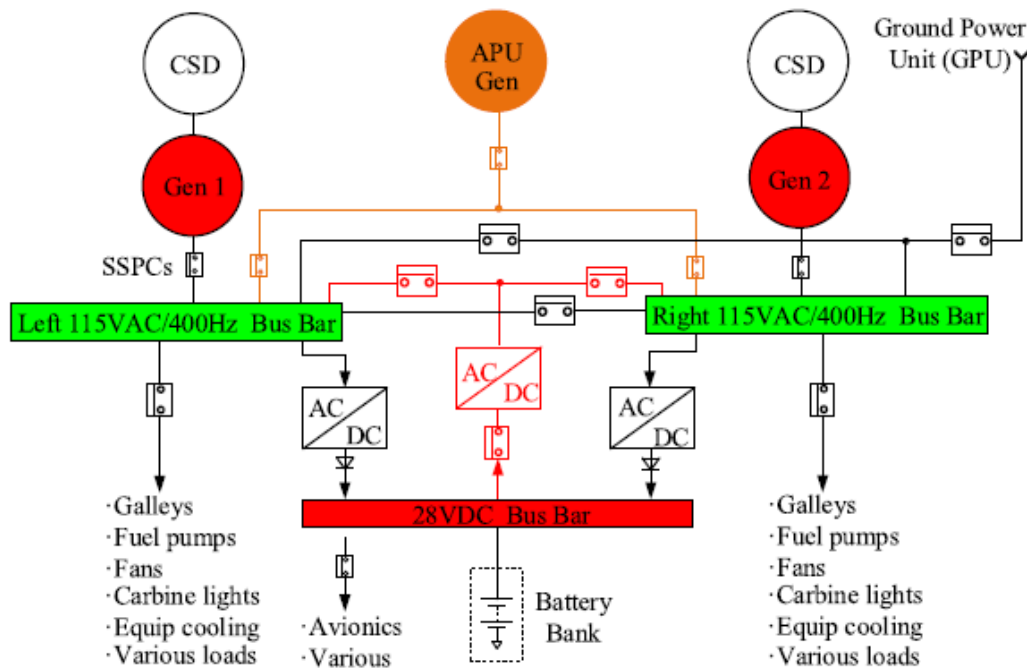
Fig. 7   Constant frequency distribution scheme
Source: [20]

The auxiliar power unit (APU) provides power, hydraulic pressure and air conditioning while the engines are off. Furthermore, it provides power to start the engines, to turn the compressor off and to keep critical systems running during power losses in flight.

3.4.1.1. Frequency values justification

In the aircraft industry, weight optimization is essential. That is why AC generators are used instead of DC generators, i.e., they can generate the same power while being lighter. Another interesting topic is the reason of using 400 Hz. To explain it, the transformer EMF equation must be analysed.

$$E = 4{,}44 \, f \, N \, \phi = 4{,}44 \, f \, N \, A \, B \qquad\qquad \text{Eq. 1}$$

$$N \, A = \frac{E}{4{,}44 \, f \, B}$$

Where E is the electromotive force of a transformer winding, f is the applied voltage frequency,

N the number of turns of the coil, A is the cross-sectional area of the transformer core, ϕ is the maximum allowable flux in Wb while B is the maximum allowable flux density.

After observing the last equation, it can be determined, for a fixed E and B, if frequency increases, the couple N A decreases. Therefore, transformer core and number of turns can be reduced as increasing the frequency.

Additionally, since the voltage or current waveforms period is higher, less capacitance is required to attenuate the peaks, in other words, to reduce the ripple. Then, fewer and smaller components for filtering are required.

Another reason of this frequency value is that 400 Hz is a feasible frequency for the generator speed. For instance, for a four-pole machine using 400 Hz, a velocity of 12000 rpm is achieved, which is a feasible value for the generator (see equation 2). Army Air Corps chose this value in 1943 and it became a mandatory standard for the US Air Force in 1959.

$$N = \frac{60\,f}{p} = \frac{60 \cdot 400\ \text{Hz}}{2\ \text{pole pairs}} = 12000\ \text{rpm} \qquad \text{Eq. 2}$$

Nonetheless, frequency is limited by the AC skin effect. It consists in the tendency of alternate current to flow near the surface of the conductor. Thus, current density is larger near the cable surface while it is limited near the core.

3.4.1.2. Voltage levels justification

Aircraft manufacturers use 28 VDC instead of other industry standards such as 24 VDC because, for a given power, if voltage is increased, current decreases. Therefore, cables cross-section can be reduced as can their weight.

The reason behind using 115 VAC or 230 VAC is that this voltage level is high enough to transmit high power over a convenient distance and low enough to avoid corona effects at altitude. It must be convenient to remember Paschen's law. Basically, it says that the breakdown voltage between two electrodes at a fixed distance decreases with the pressure. Since pressure decreases with altitude, breakdown voltage becomes smaller when altitude increases. When voltage reaches the breakdown voltage limit, air surrounding the conductor is ionized and a corona discharge can be produced. It is an undesirable effect because the

current leakage can constitute an unwanted load on the circuit. Furthermore, coronas generate gases such as ozone (O_3) nitric oxide (NO), nitrogen dioxide (NO_2) and nitric acid (HNO_3) if water vapor is present. These gases are toxic to humans and the environment and they can degrade the materials.

The next table is filled out with the advantages and disadvantages of constant frequency distribution. All the above disadvantages increase the airplane weight.

Table 1. Advantages and disadvantages of constant frequency distribution

Advantages	Disadvantages
Mature and well-known architecture.	The frequency converter has to be large enough to process all the generated power.
	Additional converters must be installed near the loads, e.g., some drivers need to vary their frequency.
	It uses a CSD. It increases weight and reduces efficiency.

3.4.2. Variable frequency distribution

In this case, the CSD is removed so the engine can be connected directly to the generator. This results in a variable frequency primary bus. Its values are typically between 360 and 800 Hz. Regarding bus voltage levels, two groups can be distinguished:

1) 115 VAC / 360 – 800 Hz and 270 VDC
2) 230 VAC / 360 – 800 Hz and ±270 VDC

F22 and F35 from Lockheed Martin and the Airbus A380 are examples of the first group while Boeing B787 is part of the second one. As discussed before, increasing the voltage leads to reduce the system weight.

An autotransformer rectifier unit (ATRU) is used to rectify the voltage and AC/AC converters are used to power constant frequency loads. Figure 8 shows a scheme of the first group. They use 270 VDC because this voltage can be directly obtained by rectifying 115 VAC via an ATRU.
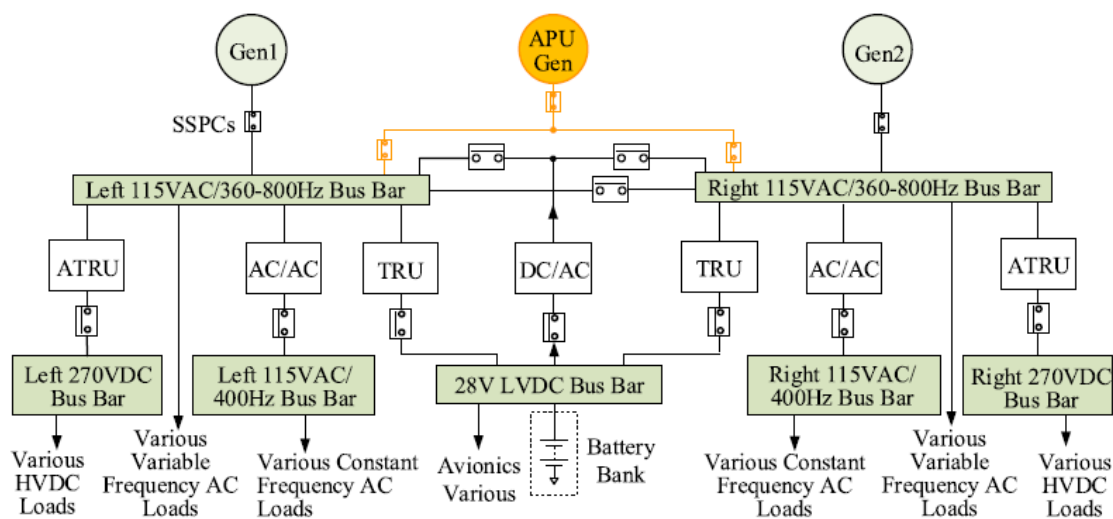
ETSEIB

Fig. 8   Variable frequency distribution scheme
Source: [20]

Table 2 summarizes the pros and cons of this architecture. All the points are related to the weight improvement.

Table 2. Advantages and disadvantages of variable frequency distribution

Advantages	Disadvantages
CSD is removed. Weight decreases while efficiency increases.	Accessory motors such as pumps and fan motors become larger if they are supplied by variable frequency.
More redundant architecture because it allows many distributed power converters. Reliability improves.	
It does not need rated-power converters connected to the generators. They can be smaller compared to constant frequency ones.	
Multiple loads can be connected directly to the variable frequency bus since most of them are resistive loads. E.g., wing ice protection, galley ovens and cargo heaters.	

4.4.3 DC distribution

The last structure mainly distributes energy using DC power (figure 9). Regarding the voltage level, it is set at ±270 VDC because it can be easily obtained by using diode rectifiers from 230 VAC. Furthermore, it allows to remove the inter-rectification stage that some drives have since there is no need to use an internal DC voltage bus. Thus, weight reduction can be achieved.

It seems that the trend for future MEAs is to use this architecture. Several research groups such as MOET EU, CleanSky project and Airbus HVDC project are studying this distribution topology.
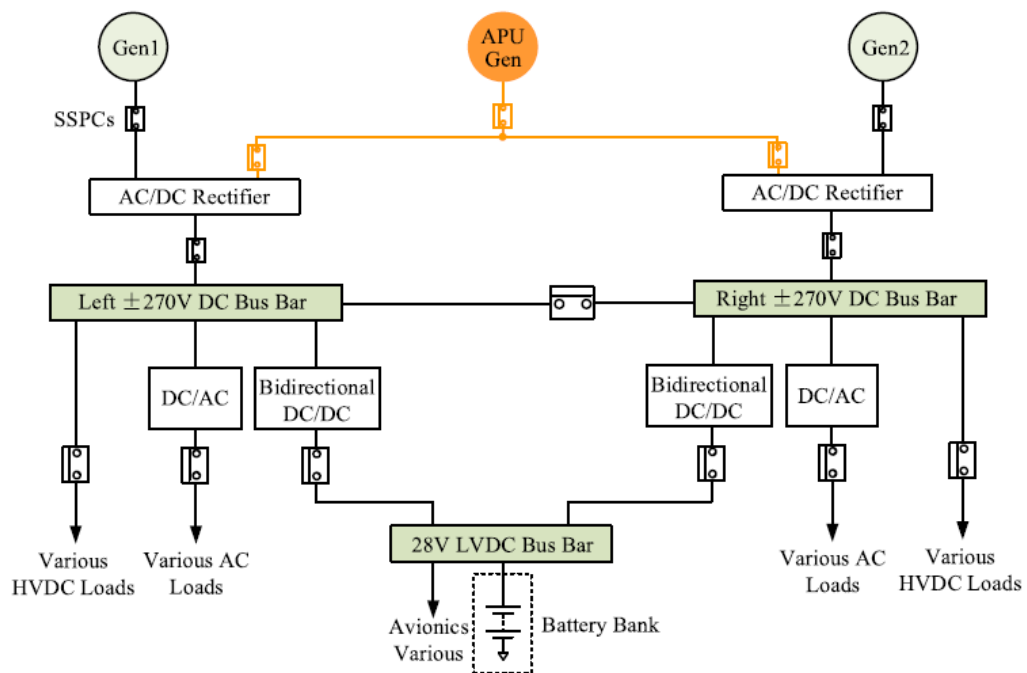

Fig. 9   DC distribution scheme

Source: [20]

Main advantages of this architecture are addressed in table 3.

Table 3. Advantages and disadvantages of DC distribution

Advantages	Disadvantages
Coupling between the main source and storage devices is easier since the last ones are DC based mainly.	Power quality and stability issues must be considered.
It only needs two cables to transmit power. The number of power converters and required cable insulation decrease.	DC faults are more difficult to isolate and extinguish compared to AC faults. These protections are more complex.
The skin effect decreases because it depends on the frequency.	Corona effect and insulation breakdown can crash the system.
The number of storage devices can be increased.	
It is easier to parallelise DC sources because they only require the same voltage amplitude, there is no need to synchronise phase and frequency.	

3.5. Wiring weight

In this sub-chapter, the best architecture regarding weight reduction is addressed. Figure 10 shows a wiring weight comparison between four different architectures. The reference weight is the heaviest type, i.e., constant frequency architecture. Following page 14 naming, EPS-A1 - EPS-A4 from the picture below are type 1, 2.1, 2.2 and 3 respectively.
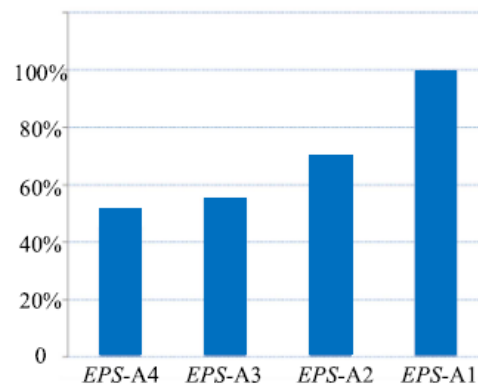
Fig. 10   Weight comparison between different power distribution topologies
Source: [20]

It can be observed that DC architecture is the lightest being approximately half of the constant frequency weight. Some reasons behind this fact are listed below:

- DC architecture does not use a CSD
- Doubling the voltage level would reduce the cable weight to approximately 35 % of the reference weight [20]
- Power density (kW/m^3) of a DC/DC converter is higher than AC converters power density because they operate at higher switching frequencies (see table 4)
- AC converters need power factor corrections and more filtering systems
- DC topologies have less power conversion stages
- DC power distribution uses two cables while AC systems use at least three

Table 4   Power weight ratio for converters
Source: [21]

Converters (with PFC)	Power to weight ratio
AC to AC	12 kg/kW
AC to DC	7 kg/kW
DC to AC	6 kg/kW
DC to DC	1 kg/kW

ETSEIB

4. Microgrid components design and simulation

4.1. Overview

The simulation is based on a Boeing B787 architecture. The plane has four generators (two per wing) but, it has been simulated a quarter part of the power system since there is only one generator. ATRU has been removed because the structure is similar to the TRU: a transformer or an autotransformer followed by an uncontrolled twelve-pulse rectifier.

Microgrid structure can be seen in figure 11. Variable speed generator (VSG) powers all buses: variable frequency 230 VAC, constant frequency 115 VAC and 28 VDC. There are two conversion stages upstream last two buses: an AC/AC converter and a transformer rectifier unit before 115 VAC and 28 VDC buses respectively.
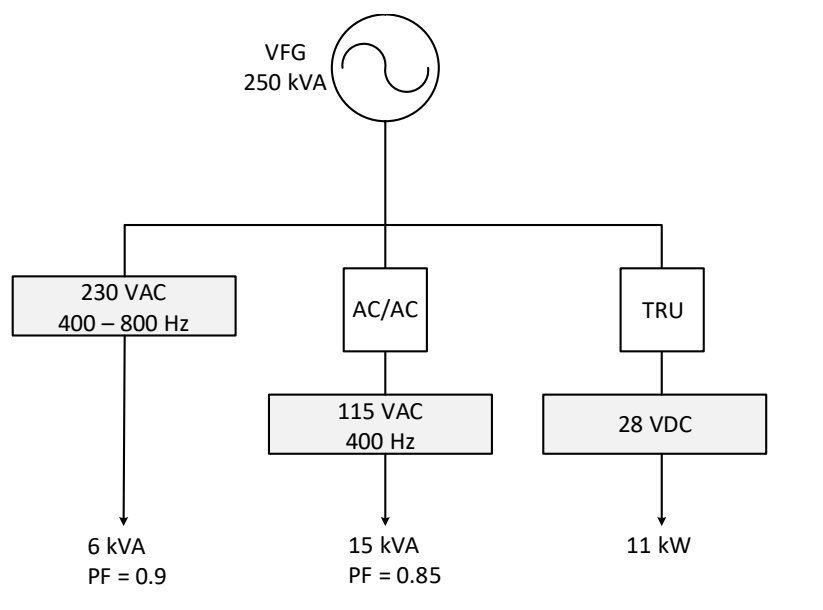

Fig. 11   Microgrid Scheme

Regarding the loads, their values have been inspired by simulation values of [1] and [2]. Low voltage DC load is larger than normal since there is not any ±270 VDC load after ATRU removal.

4.2. Generator

A microgrid scheme has been created to clarify the location of every component described in this chapter. The element of study has been marked in red (figure 12).
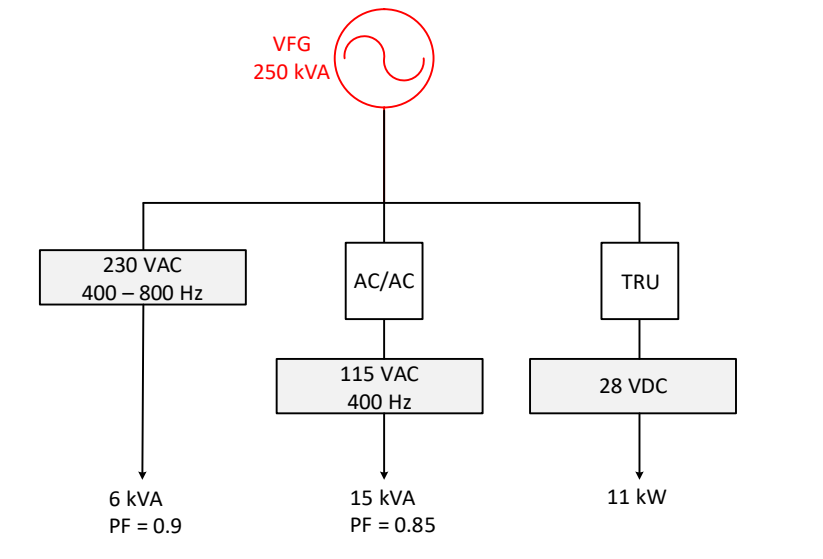

Fig. 12   Microgrid Scheme

VSVF generators used in a Boeing B787 are three-level brushless generators. As seen in figure 13, the variable speed turbine is attached to a permanent magnet (rotor). When it spins, it excites the pilot exciter (stator), which after a voltage regulator, it powers the main exciter (stator). This last element is responsible for providing exciting current to the main generator (stator) through a rotating rectifier assembly (rotor). The loop is closed measuring the output voltage and the generator control unit controls the voltage regulator by adjusting exciting current. Frequency is proportional to the variable speed of the rotor.
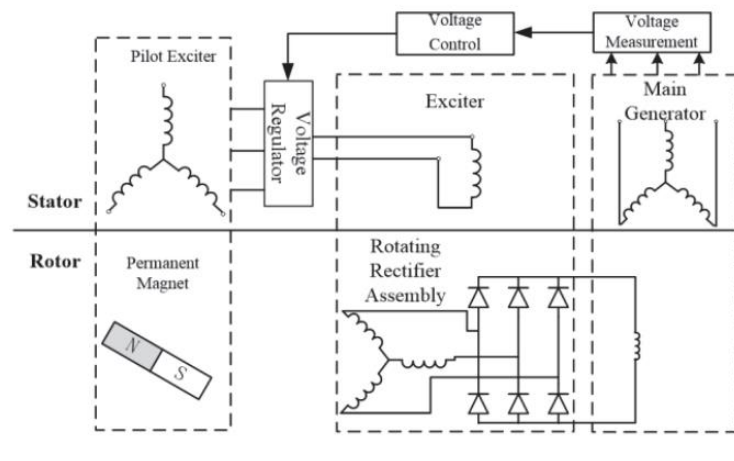
Fig. 13   Three-level Brushless Generator
Source: [1]

4.2.1. Exciter model

The Simulink model used is IEEE type AC5A. It has been chosen because it simulates a simplified brushless excitation system where the regulator is supplied from a permanent magnet generator with a rotating rectifier.

4.2.2. Generator model

For this simulation, Simplified Synchronous Machine block has been used. It implements a mechanical system described by the equations below. Basically, the speed variation with respect to speed operation can be computed integrating the resulting torque and then dividing it two times by the inertia constant. Generator output voltage is controlled by the exciter voltage.

$$\Delta\omega(t) = \frac{1}{2H} \int_0^t (T_m - T_e) - K_d \Delta\omega(t) \, dt \qquad \text{Eq. 3}$$

$$\omega(t) = \Delta\omega(t) + \omega_0 \qquad \text{Eq. 4}$$

Where:

$$\Delta\omega = Speed\ variation\ with\ respect\ to\ speed\ of\ operation$$
$$H = constant\ of\ inertia$$
$$T_m = mechanical\ torque$$
$$T_e = electromagnetic\ torque$$
$$K_d = damping\ factor\ representing\ the\ effect\ of\ dampler\ windings$$
$$\omega(t) = mechanical\ speed\ of\ the\ rotor$$
$$\omega_0 = initial\ speed$$

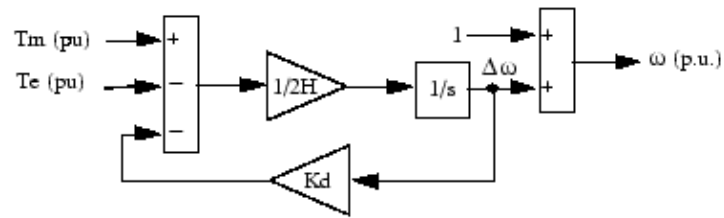The above equations can be expressed in a block system (figure 14).

Fig. 14   Generator Block System
Source: Simulink Help

The complete system is shown in figure 15, it has been based on MATLAB example *power_aircraft_distribution* but replacing the original exciter for the AC5A block. Signal 1 block represents variable speed of the turbine in min^{-1}, after the conversion to rad/s it enters to w terminal of the Simplified Synchronous Machine Block. A parasitic resistive load is connected in parallel to run the simulation without any debugging issues and P.O.R and CTA is just a measurement block. The parameters of the system are displayed in appendix B.

Fig. 15   Generator block system
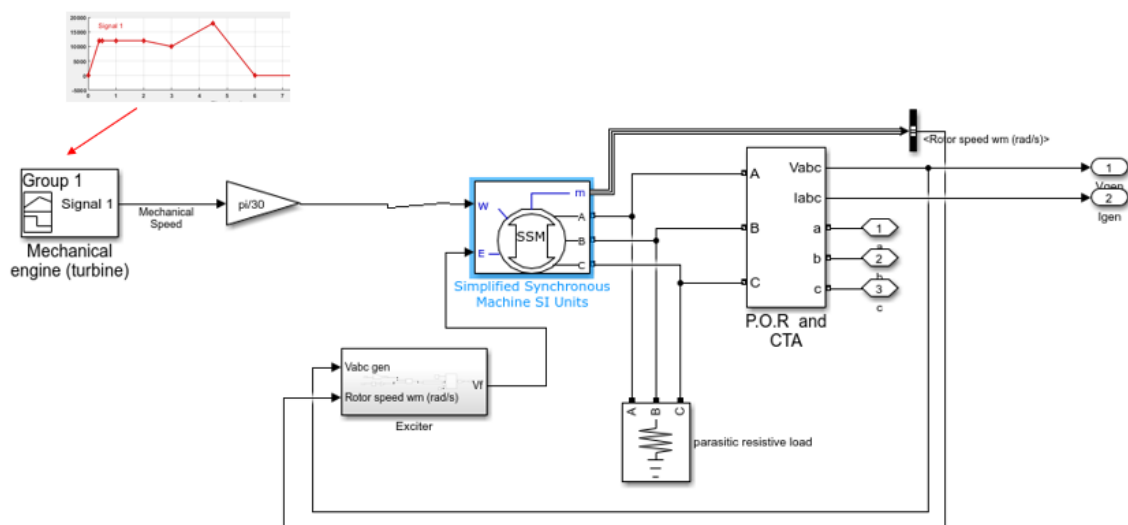
Regarding the exciter, figure 16 shows what is inside the block. Basically, three-phase output voltage is transformed to dq0 coordinates using the position of the rotor. The modulus of the transformed voltage, together with the reference in p.u., enter to AC5A block. This last element is responsible for controlling output voltage of the four-pole machine via field voltage.
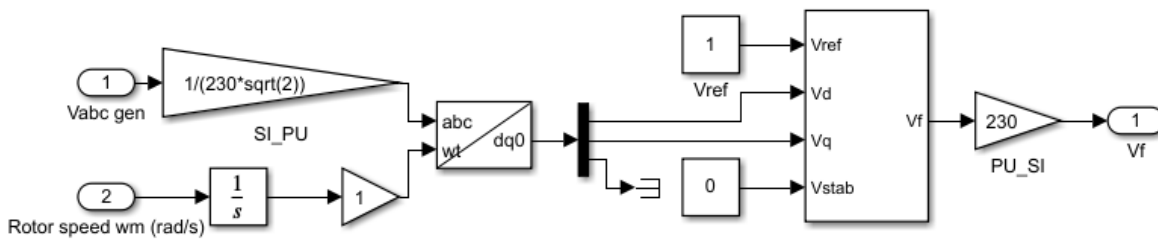
Fig. 16   Exciter block system

4.3. Transformer Rectifier Unit (TRU)

The next element to design is the transformer rectifier unit (figure 17).
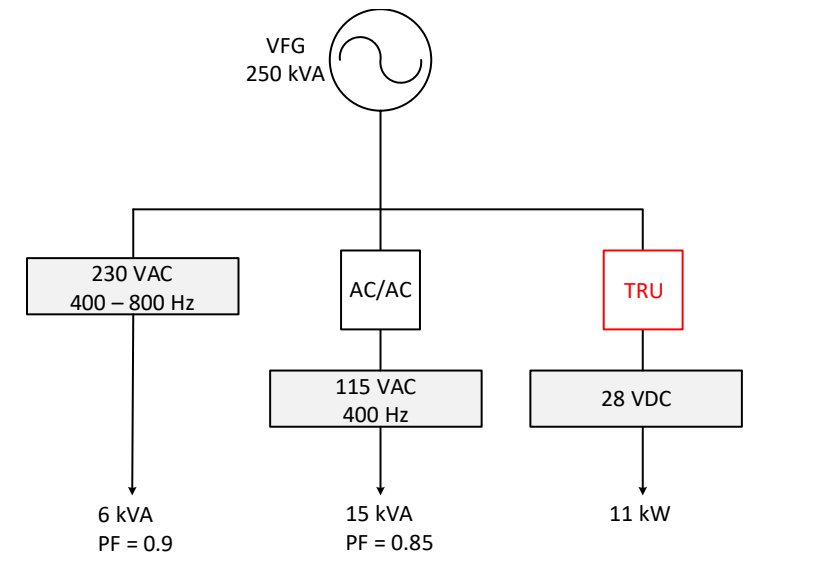
Fig. 17   Microgrid Scheme

Boeing B787 uses a TRU to convert a three-phase AC voltage to a DC voltage. It consists of two six-pulse rectifiers in parallel connected to a common DC bus. To obtain twelve pulses, it is necessary to phase shift 30° one six-pulse current waveform from the other. A transformer with one primary coil and to secondary windings is used for this purpose. The primary winding is connected in wye provided one secondary coil is wired in wye and the other in delta and vice versa (figure 18).
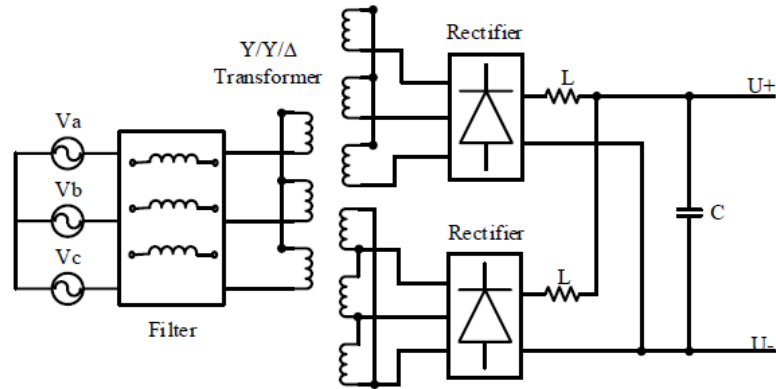
Fig. 18   12-pulse rectifier

Source: [2]

Phase-shifting waveforms eliminates both 5th and 7th harmonic and reduces current THD between 10 % and 15 % compared to a six-pulse rectifier but the cost is higher because it requires more diodes and a three-winding transformer [7].

Figure 19 shows the harmonic content of a six, twelve and twenty-four-pulse rectifier. It can be seen the 5th and the 7th harmonics are not neglectful for a six-pulse rectifier since they are over 25 % and 6 % of the fundamental current value respectively. Furthermore, a twelve-pulse rectifier can reduce significantly all the harmonics except the 11th and the 13th.

Fig. 19   Harmonic content of a 6, 12 and 24-pulse rectifier

Source: [7]

For a 12-pulse rectifier (TRU), assuming the same equation as a 6-pulse rectifier, input voltage to obtain 28 VDC can be calculated. The equations are extracted from [1] and [2].
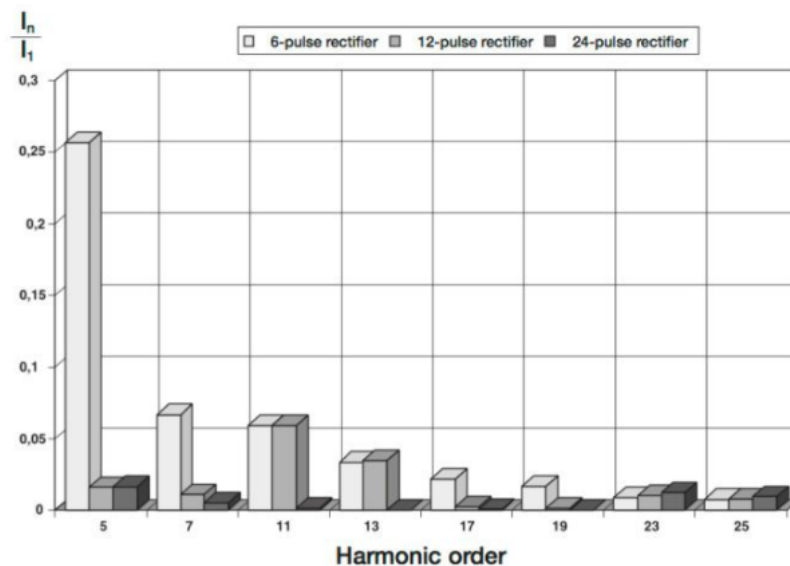
$$V_l = \frac{\pi}{3\sqrt{2}} V_{dc}$$

Eq. 5

$$V_{dc} = 28 \, V \rightarrow V_l = 20,73 \text{ VAC}$$

Where V_l is the line voltage phase to phase

With a conversion efficiency of 95 %:

$$V_l = \frac{20,73}{0,95} \cong 22 \text{ VAC}$$

Therefore, the transformer has to decrease the voltage from 230 $V_{ph\text{-}ph}$ to 22 $V_{ph\text{-}ph}$.

4.3.1. Output filter design

An inter-phase reactor connects both rectifiers in parallel before the DC bus to address the unbalanced voltage problem. When the output voltages of the rectifiers are not equal, this inductance compensates the difference.

First, I_{DC} and R_{ef} must be calculated:

$$I_{d \, min} = minimum \, load \, current \cong 1 \, \% \, DC \, curent$$

$$R_{ef} = Equivalent \, resistance \, on \, the \, DC \, side$$

Being P_{DC} = 11 kW and V_{DC} = 28 V:

$$I_{DC} = \frac{P_{DC}}{V_{DC}} = \frac{11000 \text{ W}}{28 \text{ V}} = 392,86 \text{ A}$$

Eq. 6

$$I_{d \, min} = 0,1 \, I_{DC} = 39,29 \text{ A}$$

Eq. 7

$$P_{DC} = \frac{V_{DC}^2}{R_{ef}} \rightarrow R_{ef} = \frac{V_{DC}^2}{P_{DC}} = 0,07127 \, \Omega$$

Eq. 8

Then, the inter-phase reactor and the DC capacity can be obtained for the critical frequency (400 Hz):

ETSEIB

$$L = \frac{\sqrt{2}\left(1 - \frac{\sqrt{3}}{2}\right) V_l}{3\omega I_{d\ min}} = 14{,}07 \ \mu\text{H} \qquad \text{Eq. 9}$$

$$C = \frac{2}{2\pi f R_{ef}} = 11{,}17 \ \text{mF} \qquad \text{Eq. 10}$$

As seen in figure 19, a 12-pulse rectifier requires an input filter because it introduces harmonics into the grid, in particular, the 11th and the 13th [3]. Since it works in a variable frequency system, it does not make sense to design a tunned filter for a specific frequency. Thus, an inductor filter of 1 mH can be used. Figure 20 shows TRU block system in Simulink.
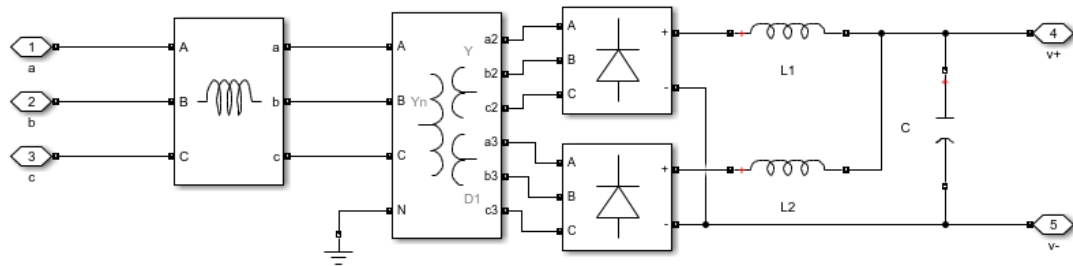

Fig. 20   TRU block system

4.4. AC/AC converter

4.4.1.   Overview

The next element to design is the AC/AC conversion step (figure 21). As figure 22 shows, it is composed by a transformer followed by an AC/AC converter with its input and output filters.
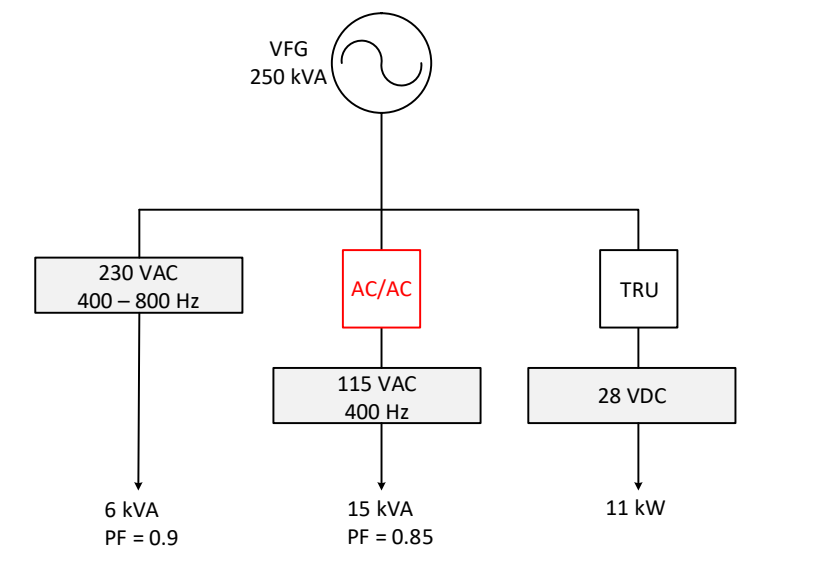
Fig. 21   Microgrid Scheme
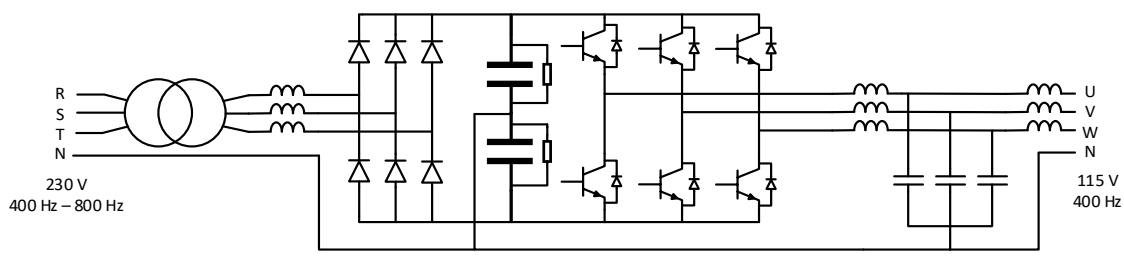
Fig. 22   AC/AC conversion stage

The purpose of the AC/AC converter is to supply 115 V 400 Hz to constant frequency loads. It has to convert 230 V_{ph-ph} 400 Hz - 800 Hz from the variable frequency bus to 115 V_{ph-ph} 400 Hz. To do that, it converts the power to DC in an intermediate step and then it transforms the power to AC again. The conversion chain is the following: transformer, input filter, uncontrolled rectifier, DC bus, controlled inverter and output filter.

4.4.2. Bus design

As regards specifications, DC bus voltage level must be higher than both input and output voltage peak. Input voltage peak level is 325,27 V while the output one is 162,63 V. Therefore, a DC voltage bus rated at 500 V will suit this application.

The bus is composed by two capacitors connected in series and the neutral point is located in the middle of the bus, i.e., between both capacitors. Figure 23 shows the converter scheme.
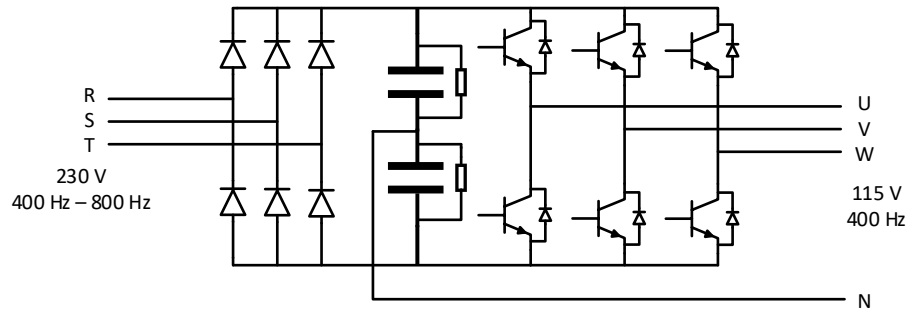
Fig. 23   AC/AC converter

The AC to DC converter is a six-pulse diode rectifier while DC to AC converter is a universal bridge IGBT inverter controlled with SPWM technique. Capacitor capacitance is 5 mF and every capacitor has a 50 kΩ resistor connected in parallel to equilibrate the bus voltage. When bus capacitors are charged, all current flows through these resistors and they impose the same voltage drop in every capacitor since they constitute a voltage divider (figure 24). Moreover, they will discharge the bus when the converter is turned off.
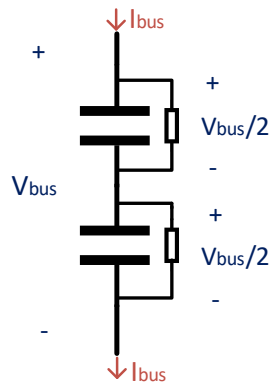
Fig. 24   Bus and balancing resistors

The law every capacitor follows during its discharge is:

$$\Delta t = -C\,R\,\ln\left(\frac{V_f}{V_i}\right)$$

Eq. 11

Where Δt is the required discharging time, V_i and V_f are initial and final voltages respectively, C is the capacitance of one bus capacitor and R is the resistance of one discharging resistor.

For instance, the required time to discharge the capacitor from 250 V to 20 V is calculated below. It requires approximately 10,5 minutes to discharge using a 5 mF capacitor and a 50 kΩ resistor.

$$\Delta t = -5 \cdot 10^{-3} \cdot 50 \cdot 10^{3} \cdot ln\left(\frac{20}{250}\right) \approx 631 \ s$$

### 4.4.3.   Input filter

It is known that in a 6-pulse diode rectifier, only the odd harmonic voltage that cannot be divided by 3 can occur, i.e.: 5, 7, 11, 13, 17, 19, 23, 25, 31… [4]. Since the grid frequency is variable, there is no reason to design a tuned filter. A simple 5 mH inductor placed before the six-pulse rectifier can be used as a filter.

4.4.4.   Six-pulse rectifier

As explained before, a six-pulse rectifier is used to convert a three-phase AC voltage to DC voltage. In this topology, the ripple frequency is 6 times higher than the fundamental grid frequency. The natural commutation order, powering it with a balanced three-phase grid, is 1,2,3,4,5 and 6 (numbering the diodes as shown in figure 25). Each diode conducts during 120° and the DC voltage amplitude after the conversion is theoretically equal to the peak line input voltage. Current waveforms are similar to the voltage ones. However, there are two main differences, they switch off and on every 120° and magnitude depends on the load value (figure 26).
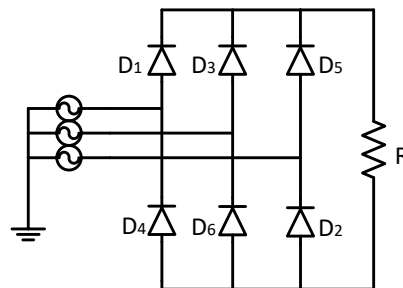
Fig. 25   Six-pulse rectifier
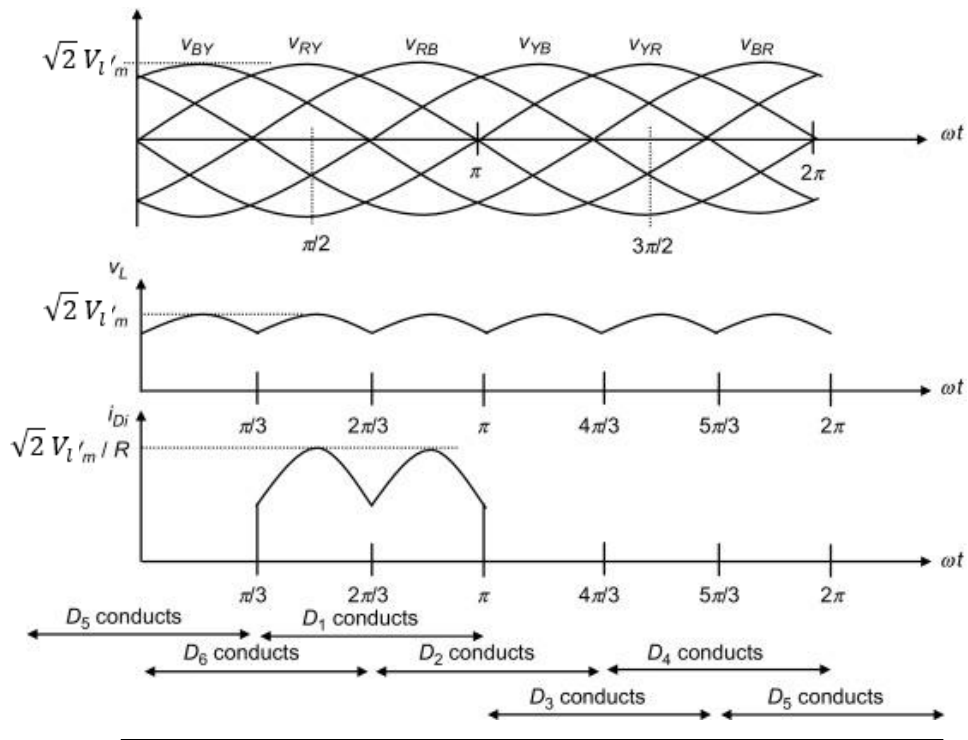
Fig. 26   Six-pulse rectifier waveforms
Source: [5]

4.4.5. Transformer ratio calculations

To calculate the DC voltage, the area of this ripple must be found and then divided by the period in radians (see figure 26 above).

$$V_{DC} = \frac{6}{2\pi} \int_{\frac{\pi}{3}}^{\frac{2\pi}{3}} \sqrt{2}\, V_l \sin\theta \; d\theta$$

Eq. 12

The equation below is obtained. It relates input AC voltage with output DC voltage.

$$V_{DC} = \frac{3\sqrt{2}\, V_l}{\pi}$$

Eq. 13

Being $V_{DC\,Bus}$ equal to 500 V, line voltage must be 370,24 $V_{ph\text{-}ph}$.

$$V_l = \frac{\pi}{3\sqrt{2}}\, V_{DC} = 370{,}24 \text{ VAC}$$

Assuming an efficiency of the 95 %, input voltage must be around 390 $V_{ph\text{-}ph}$.

$$V_l = \frac{370,24}{0,95} \cong 390 \text{ VAC}$$

Finally, a step-up transformer has to convert 230 V$_{ph\text{-}ph}$ to 390 V$_{ph\text{-}ph}$ to obtain the required DC output voltage level to power the DC bus.

4.4.6. Control and pulse generation

4.4.6.1. Controller

A discrete PID controller has been used to control output voltage. Figure 27 shows the block diagram of the control process. First, the reference signal is generated, then error signal is generated after comparing the reference with the output voltage (filtered). The error enters the controller and it is multiplied by k$_P$, k$_I$ and k$_D$ to generate the control action. This signal is divided by $\frac{V_{bus}}{2}$ to obtain the compare value. This value is compared with the carrier signal to generate the pulses to trigger the IGBTs. The loop is closed after measuring filtered output voltage.
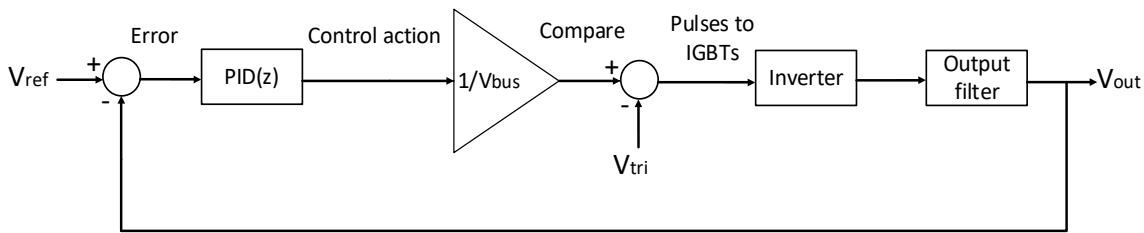
Fig. 27   Inverter control block system

Where V$_{ref}$ is the voltage reference i.e., a sine wave of 400 Hz with an amplitude of $\frac{115\sqrt{2}}{\sqrt{3}}$ V (phase to neutral). V$_{tri}$ is the ± 1 V triangular (carrier) signal of 60 kHz. V$_{out}$ is the filtered output voltage (phase to neutral). Sampling time of the controller is the same as simulation time: T$_s$ = 1 µs. The controller equation is the following:

$$C(z) = k_P + k_I T_s \frac{1}{z-1} + k_D \frac{1}{T_s} \frac{z-1}{z} \qquad \text{Eq. 14}$$

Where T_s is the sampling time and k_P, k_I, k_D are proportional, integral and derivative constants respectively.

Table 5 summarizes the controller parameters. Controller constants have been found empirically.

Table 5   Controller parameters

Parameter	Value
k_P	25000
k_I	100
k_D	0,1
T_s	1 µs

It must be considered that output limits are set to $\pm \frac{V_{bus}}{2}$ to avoid the windup effect of the integral controller. If the anti-windup had not been implemented, system response would be really slow after a large accumulated error.

4.4.6.2. Pulse generation

As explained before, the inverter is a universal bridge constituted of six IGBTs with an antiparallel diode connected between its terminals. To trigger the transistors, a sinusoidal PWM technique (SPWM) is used. It is based on comparing a sine reference wave of the desired output frequency with a triangular carrier wave of a higher frequency. Both obtained pulses and the inverted signal are sent to the top and bottom IGBTs of an inverter leg. To avoid short-circuiting the bus, they cannot be equal at the same instant, hence one signal is the inverted version of the other.

Figure 28 shows the principle of this technique, in the top picture, the comparison between the reference sinusoidal wave with the triangular carrier wave can be seen. In this case, amplitude modulation index m_a is 0.8. It is defined as the ratio between the magnitude of the maximum voltage of the sinusoidal reference and the triangular signal (carrier wave).
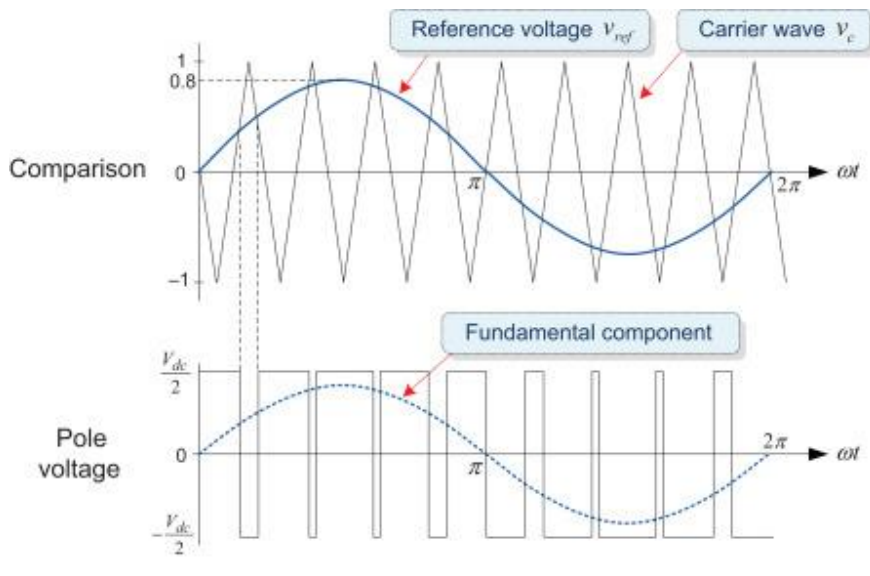
Fig. 28   SPWM technique
Source: [11]

As seen in figure 29, voltage amplitude increases proportionally with m_a until it reaches the value of 1 (lineal region). When $1 \leq m_a \leq 3,24$, in the overmodulation region, voltage amplitude also increases but not in a linear way. After $m_a \geq$ the output signal is a square wave. In this simulation m_a is 1 since the controller output is saturated at $\pm V_{Bus}$.

The second diagram of figure 28, shows the resultant output wave which is a bipolar PWM signal between $\pm \frac{V_{bus}}{2}$. The average value of the output waveform is a sinusoidal signal.
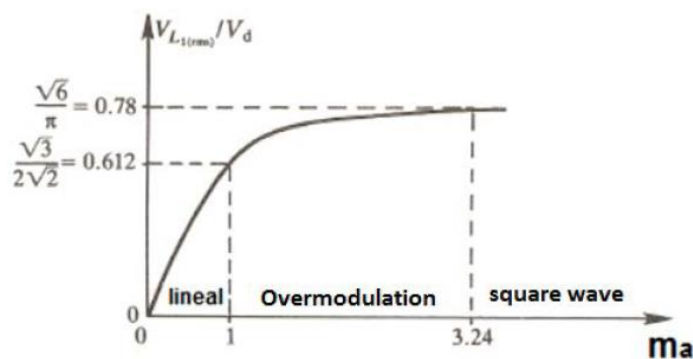
Fig. 29   Amplitude Modulation Index zones
Source: [12]

Figure 30 shows the full Simulink implementation of the transformer, inverter, control and filtering.
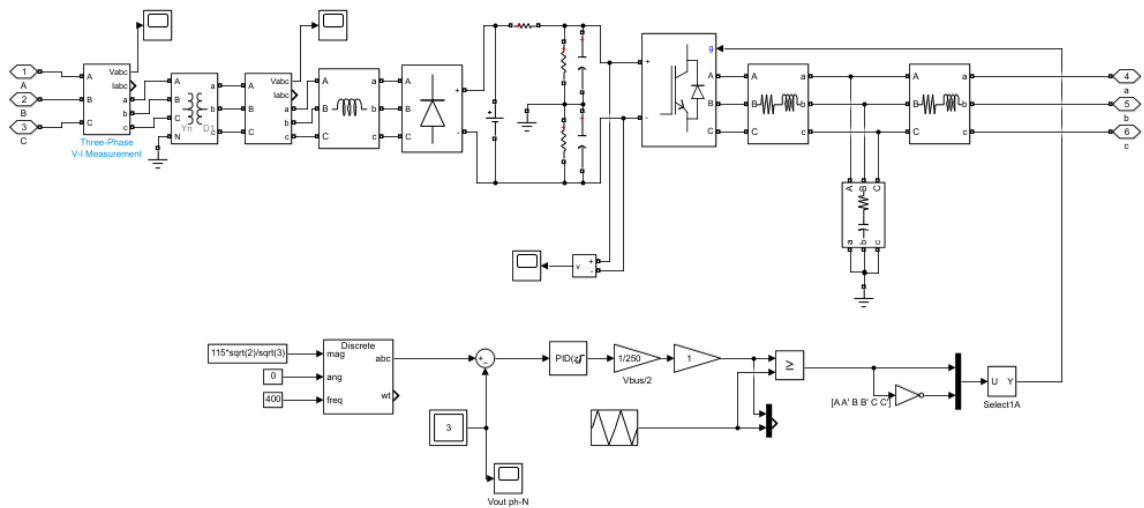
Fig. 30   AC/AC conversion stage block system

4.4.7.   Output filter

An LCL filter is necessary to smooth output voltage signal. An LCL filter has been chosen since they require less rating inductor and capacitor to reduce the same amount of distortion from a voltage or current wave compared to LC filters [8]. Figure 31 shows LCL filter topology and the notation used to refer to its components.
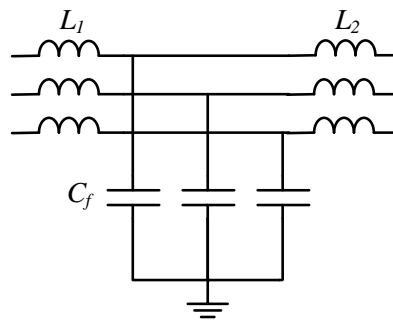
Fig. 31   AC/AC converter output filter

The LCL filter has been designed following the recommendations of [6]. First of all, maximum current ripple must be computed. Following DO 160-G standard, for a 115 V system with a load power greater than 1 kVA, the ratio between current ripple and rated power shall not exceed 0,14.

i.e.

$$\frac{\Delta I_{max}}{I_R} \leq 0,14$$
<div align="right">Eq. 15</div>

The AC load value is 15 kVA with a power factor of 0,85.

To calculate the maximum current ripple, rated current must be found.

$$\begin{cases} S = 15 \text{ kVA} \\ cos\varphi = 0,85 \\ V = 115 \text{ V} \end{cases} \rightarrow I_R = \frac{S/3}{V/\sqrt{3}} = 75,31 \text{ A}$$
<div align="right">Eq. 16</div>

Then, the maximum current ripple can be calculated:

$$\frac{\Delta I}{I_R} \leq 0,14 \rightarrow \Delta I_{max} = 10,54 \text{ A}$$

Following the methodology described in [6]:

$$L_1 \geq \frac{V_{DC}}{6 \cdot f_{sw} \cdot \Delta I_{max}} \geq 131 \text{ μH} \rightarrow 135 \text{ μH}$$
<div align="right">Eq. 17</div>

Where V_{DC} and f_{sw} are the bus voltage and the inverter switching frequency with values of 500 V and 60 kHz respectively.

To calculate the capacitor value, these equations are used:

$$C_b = \frac{1}{\omega_g \cdot Z_b}$$
<div align="right">Eq. 18</div>

$$Z_b = \frac{E_n^2}{P}$$
<div align="right">Eq. 19</div>

Where C_b is capacitance base value, ω_g is output frequency, Z_b is impedance value, E_n is phase to phase effective voltage and P is active power.

Capacitor value is limited by the reduction of the power factor (less than 5 %) in the rated capacity.

$$C_f \leq 0,05 \, C_b$$
<div align="right">Eq. 20</div>

Merging above equations, the capacitor value can be computed:

$$C_f \leq 0.05 \, \frac{P}{2\pi f_g \cdot E_n^2} \leq 19.18 \, \mu F \rightarrow 20 \, \mu F \qquad \text{Eq. 21}$$

The following table summarizes the variable values:

Table 6   Output filter boundary conditions

Variable	Value
P	12,75 kW
f_g	400 Hz
E_n	115 V

Then, the second inductance will be determined by the attenuation factor k_a. Choosing an attenuation of 20 % ($k_a = 0.2$):

$$L_2 = \frac{\sqrt{\frac{1}{k_a^2} + 1}}{C_f \cdot \omega_{sw}^2} = 2.11 \, \mu H \rightarrow 2.2 \, \mu H \qquad \text{Eq. 22}$$

In order to avoid resonance problems with the filter, the resonance frequency of the filter should be between 10 times the output frequency and half of the switching frequency.

$$f_{res} = \frac{\sqrt{\frac{L_1 + L_2}{L_1 \, L_2 \, C_f}}}{2\pi} = 24.19 \, \text{kHz} \qquad \text{Eq. 23}$$

$$10 f_g < f_{res} < \frac{1}{2} f_{sw}$$

$$4 \, \text{kHz} < f_{res} < 30 \, \text{kHz}$$

The resonance frequency fulfils the condition.

Table 7 summarizes inductor and capacitor values used in the simulation.

ETSEIB

Table 7   Output filter parameters

Element	Value
L_1	135 µH
L_2	2,2 µH
C_f	20 µF

4.5. Loads

The next simulation item to configure are the loads (figure 32).
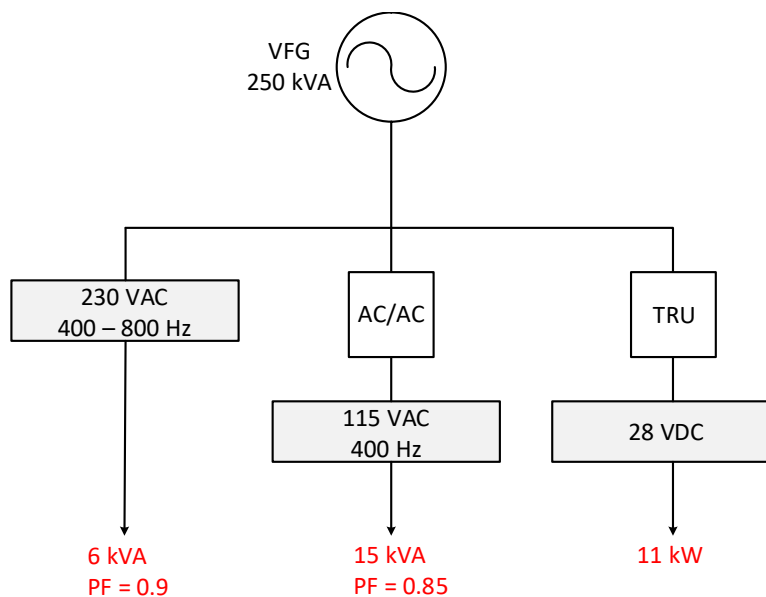
Fig. 32   Microgrid Scheme

The model has three loads: two inductive loads are connected to the variable and constant frequency buses and one resistive load is powered by the DC bus. Table 8 summarizes load values. These values are close to the ones used in [1] but, as explained before, low voltage DC load is larger since there is not any ±270 VDC load after ATRU removal.

Table 8   Load values

Variable Frequency Bus Load	Constant Frequency Bus Load	DC Bus Load
6 kVA	15 kVA	11 kW
cosφ = 0,9	cos φ = 0,85	

5. Simulation and standard checking

Industrial standards are necessary and mandatory to ensure the correct operation during the flight despite adverse boundary conditions. As figure 33 shows, there are standards for safety assessment, software, hardware, test procedures, electrical characteristics and such. Since the only open standard for electrical power, aircraft characteristics and utilization is a military standard (MIL-STD-704F), an environmental conditions and test procedures standard (DO-160G) has been used. It is useful because it shows rated and limit values for some electrical variables.

Fig. 33   Industrial standards in aircraft
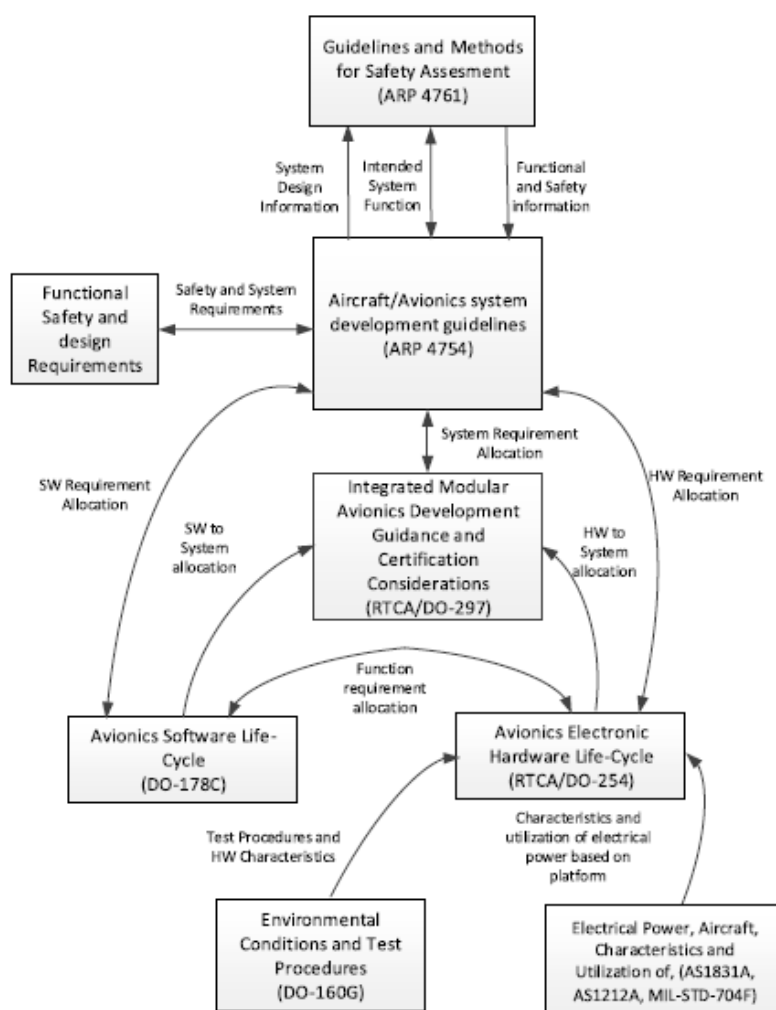Source: [16]

These standards are accepted by four organizations:

1) *RTCA:* Radio Technical Commission for Aeronautics.

2) *EUROCAE:* European Organisation for Civil Aviation Equipment.

3) *IEEE:* Institute of Electrical and Electronics Engineers.

4) *SAE:* Society of Automotive Engineers.

5.1. Harmonic analysis

The next step regarding DO 160 G compliance test is the harmonic analysis. As regards voltages, maximum voltage total and individual harmonic distortion must be checked. However, for the currents, limits for every harmonic must be checked. The model works with a wide frequency architecture (400 – 800 Hz), so maximum voltage THD and IHC must be under 10 % and 8 % respectively (tables 9, 10, 11).

Table 9   Hamonic voltage limits
Source: [DO-160G]

Equipment category	Maximum voltage total harmonic distortion (*)	Maximum voltage individual harmonic content (*)
A(CF) and A(NF)	8 %	6 %
A(WF)	10 %	8 %

Table 10   Harmonic Current Limits
Source: [DO-160G]

Harmonic Order	Limits
3rd, 5th, 7th	$I_3 = I_5 = I_7 = 0.02\, I_1$
Odd Triplen Harmonics (h = 9, 15, 21, ..., 39)	$I_h = 0.1\, I_1 / h$
11th	$I_{11} = 0.1\, I_1$
13th	$I_{13} = 0.08\, I_1$
Odd Non Triplen Harmonics 17, 19	$I_{17} = I_{19} = 0.04\, I_1$
Odd Non Triplen Harmonics 23, 25	$I_{23} = I_{25} = 0.03\, I_1$
Odd Non Triplen Harmonics 29, 31, 35, 37	$I_h = 0.3\, I_1 / h$
Even Harmonics 2 and 4	$I_h = 0.01\, I_1 / h$
Even Harmonics > 4 (h = 6, 8, 10, ..., 40)	$I_h = 0.0025\, I_1$

Table 11   Harmonic Current Limits

Harmonic Order	Limits [% fundamental]
3	2
5	2
7	2
9	1,11
11	10
13	8
15	0,67
17	4
19	4
21	0,48

The harmonic study has been done for one of the three phases until the 22nd harmonic. Different values of frequency have been used: 400 Hz, 600 Hz and 800 Hz. Bear in mind that y-axis units are the magnitude calculated as a percentage of the fundamental value. All the simulations have been done using 1µs as a sample time. Table 12 summarizes all the simulations done. It is filled with every magnitude value (percentage of the fundamental value). Voltages, currents and FFT analysis plots can be found in appendix A.

ETSEIB

Table 12   Simulated THD

Frequency	230 VAC Bus		115 VAC Bus	
	Voltage	**Current**	**Voltage**	**Current**
400 Hz	1,92	2,13	0,14	0,01
600 Hz	1,56	1,58	0,14	0,01
800 Hz	1,72	1,49	0,15	0,02

Every voltage and current measure are under the limits for every harmonic (IHC) and the total harmonic distortion (THD), so the model fulfils harmonic checking.

5.2. Rated values check

As written in DO 160 – G, AC voltage values must be between 244 V_{rms} and 200 V_{rms} for a wide frequency system (360 Hz - 800 Hz) rated at 230 V_{rms}. However, if the rated voltage is 115 V_{rms}, these values must be divided by 2. The average DC value can go from 30,3 V to 22,0 V if rated DC voltage is 28 V.

Table 13   Rated Values Limits

Measure	Min	Max
AC Voltage (230 V)	200 V_{RMS}	244 V_{RMS}
AC Voltage (115 V)	100 V_{RMS}	122 V_{RMS}
DC Voltage (28 V)	22 $V_{average}$	33,3 $V_{average}$

The measures have been summarized in table 14. It can be observed that they fulfil the requirements. As frequency increases, DC voltage level decreases, being 800 Hz the critical case with a value of 22,7 V which is close to the lower limit (22 V).

ETSEIB

Table 14   Simulated Rated Values

Bus Voltage [Vrms or Vavg]				
Bus Type/Frequency	**400 Hz**	**600 Hz**	**800 Hz**	**Limits**
230 VAC	234	232,2	229,3	[244; 200]
115 VAC	114,6	115,7	114,9	[122; 100]
28 VDC	27,8	25,5	22,9	[22; 33,3]

5.3. Ripple check

As regards DC ripple, the limits can be seen at table 15. For voltage ripple, two cases must be considered. If the equipment voltage is greater or equal than 22 V, ripple must be under 4 V_{p-p}. Otherwise, if equipment voltage is lower than 22 V, maximum voltage ripple is 2 V_{p-p}. Finally, DC current ripple has to be under 0,07 ($I_{p-p}/I_{dc\,max}$) for 28 VDC systems with a combined power greater than 1 kW. Figure 34 shows maximum and minimum values for both DC load voltage and current.

Table 15   DC Ripple Limits

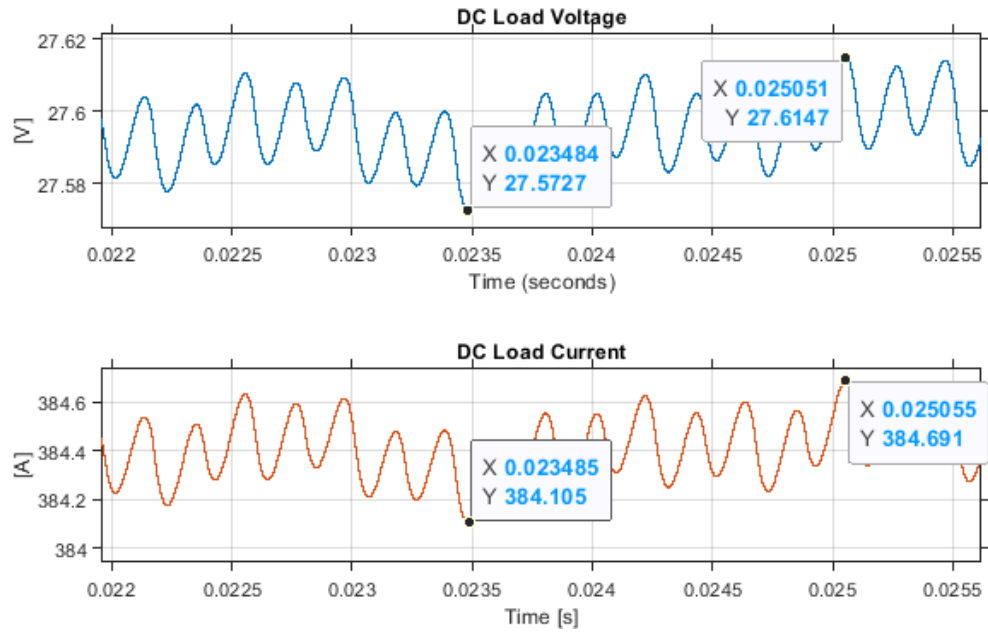| **Measure**	**Limit**
DC Voltage ripple	4 V_{p-p}
DC Current Ripple	0,07 $\Delta I/I_{DC\,max}$

ETSEIB

Fig. 34   DC ripple waveforms

Voltage ripple value (0,042 V_{p-p}) is far below the limit (4 V_{p-p}). To check whether current ripple is under the limit, it is necessary to calculate it using the formula from table 15. Current ripple fulfils the specifications again since it is lower than 0,07 $\Delta I/I_{DC\ max}$.

$$\frac{\Delta I}{I_{DC\ max}} = \frac{0,59\ \text{A}}{384,69\ \text{A}} = 0,0015\ \leq 0,07 \qquad\qquad \text{Eq. 24}$$

6.   MEA protection

Electrical protection devices are crucial in aircraft power systems in order to isolate the faults and protect every component and load. In this chapter, a circuit breaker is proposed, discussed and simulated for both AC and DC microgrids.

6.1. DC protection

6.1.1.   Overview and selection

In spite of the mentioned DC microgrid advantages, its protection is actually challenging. Since there is not naturally occurring zero crossing current, arcs are more sustained and they last longer than AC ones.

The chosen topology is a bidirectional solid-state circuit breaker because it mostly uses full-controllable semiconductors and it has a shorter turning off time compared to mechanical circuit breakers. Bidirectionality is interesting since the DC bus can be connected to a battery. Many studies have been done with thyristor-based solid-state circuit breakers. The working principle is practically the same for all these circuit breakers. They force a reverse voltage to turn the thyristor off using the capacitor discharge, thus they detect and isolate short circuit faults. [10]

Another research direction is the Z-source circuit breaker which it uses LC resonance to turn the thyristor off. The main disadvantage is that they can have an undesired triggering when a load step happens. A novel circuit breaker with a mutual inductance has been proposed in [9] to address this problem. It uses inductor's mutual inductance to turn off the thyristor.

Some topologies have been analysed in [10] by checking features like number of passive components, number of thyristors, reflected current to source and semiconductor devices and power loss when conducting. Finally, the proposed topology is shown in figure 35. The circuit has been designed by the researcher Yufeng Yang. It has more components than other topologies but, in this case, conduction losses have been prioritised. Thus, current is only flowing through one thyristor all the time except when a fault occurs. In this case the short-circuit will be isolated and any current will flow through the load. This circuit does not appear in any paper yet as it is a new design.
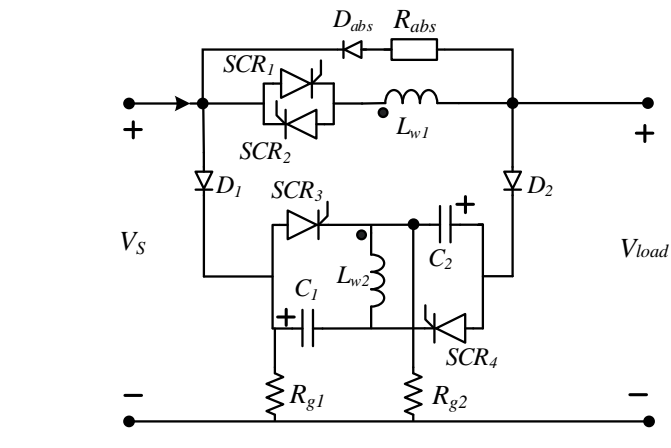
ETSEIB

Fig. 35   Proposed SSCB design

6.1.2. Working principle

First, in order to isolate the fault, C_1 must be charged. If the current flows forward (from V_s to V_{load}), energy flow path involves SCR_1, L_{w1} and the load. D_1 and SCR_1 are turned on but D_2, SCR_3 and SCR_4 are blocked. When a short-circuit occurs between positive and negative terminals, SCR_3 is triggered and C_1 discharges to L_{w2} (C1 - SCR3 - L_{w2} loop). The secondary coil will induce a reverse large current to L_{w1} due to the coupling. If reverse induced current has the same magnitude as the fault current and if it is sustained for a certain time, thyristor SCR_1 will experience a reverse voltage, thus it will turn off and isolate the short-circuit (figure 36).
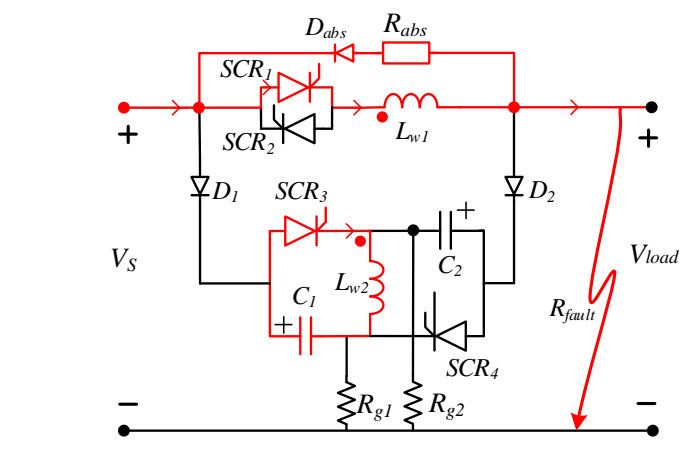

Fig. 36   DC SSCB during the fault

When short-circuit fault takes place, SCR_1, L_{w1}, R_{abs} and D_{abs} become a loop and energy absorption is achieved.

6.1.3. SSCB calculations

In order to open the SCR1, the current flowing through it has to be negative for a specific time:
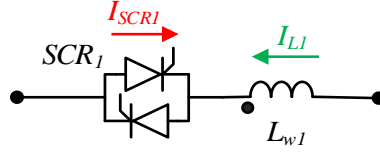

Fig. 37   Branch currents

$$I_{SCR1} = I_{TH} - i_{L_1} < 0$$

<div align="right">Eq. 25</div>

Where I_{SCR1} and i_{L_1} are the current flowing through SCR1 and L1 respectively. I_{TH} is the threshold current and it is set at 5 A.

While C1 discharges, C1-SCR3-L2-C1 loop forms an LC resonant circuit (ignoring SCR3 voltage drop). The discharging capacitor current is the same one that flows through the inductor (see figure 36).

$$i_{c_1} = i_{L_2} = n\, i_{L_1}$$

<div align="right">Eq. 26</div>

Where i_{c_1}, i_{L_2}, i_{L_1} are capacitor, secondary coil and primary coil currents and n is the turn ratio of the coupled inductor. It can be expressed as:

$$n = \frac{v_{L_1}}{v_{L_2}} = \frac{i_{L_2}}{i_{L_1}} = \sqrt{\frac{L_1}{L_2}} \rightarrow i_{L_1} = \frac{i_{C_1}}{n}$$

<div align="right">Eq. 27</div>

The differential equations for the resonant circuit and its components are the following:

$$i_{c_1} = C_1 \frac{dv_{c_1}}{dt}$$

<div align="right">Eq. 28</div>

$$v_{L_2} = L_2 \frac{di_{L_2}}{dt}$$

<div align="right">Eq. 29</div>

$$v_{L_2} + v_{c_1} = 0 \rightarrow L_2 \frac{d\left(C_1 \frac{dv_{c_1}}{dt}\right)}{dt} + v_{c_1} = 0$$

The second order equation of the resonant circuit is:

$$L_2 C_1 \frac{d v_{c_1}^{\,2}}{dt^2} + v_{c_1} = 0 \qquad \text{Eq. 30}$$

Regarding initial conditions for the capacitor just when SCR3 is triggered, initial voltage value will be the same as the voltage source and initial current will be 0 A since there is a diode-capacitor-resistor branch connected in parallel with the voltage source.

$$v_{c_1}(0) = V_s$$

$$i_{c_1}(0) = 0$$

The solution for second order equation considering initial conditions is:

$$v_{c_1}(t) = V_s \cos\left(\frac{t}{\sqrt{L_2\,C_1}}\right) \qquad \text{Eq. 31}$$

$$i_{c_1}(t) = \frac{C_1\,V_s}{\sqrt{L_2\,C_1}} \sin\left(\frac{t}{\sqrt{L_2\,C_1}}\right) \qquad \text{Eq. 32}$$

Returning to equation 25 and using the expression obtained at 27:

$$I_{SCR1} = I_{TH} - \frac{i_{c_1}}{n} < 0 \qquad \text{Eq. 33}$$

Combining equation 32:

$$I_{SCR1} = I_{TH} - \frac{C_1\,V_s}{n\sqrt{L_2\,C_1}} \sin\left(\frac{t}{\sqrt{L_2\,C_1}}\right) < 0 \qquad \text{Eq. 34}$$

Using the Taylor's expansion to the second term:

$$I_{SCR1} = I_{TH} - \frac{C_1 V_s}{n\sqrt{L_2\,C_1}} \left[\frac{t}{\sqrt{L_2\,C_1}} - \frac{1}{6}\left(\frac{t}{\sqrt{L_2\,C_1}}\right)^3 \right] < 0$$

Considering t_q is the time that I_{SCR1} must be kept negative to open the thyristor, the equation can be rewritten in this way:

$$I_{SCR1} = I_{TH} - \frac{V_s\,t_q\big(6\,C_1\,L_2 - t_q^2\big)}{6\,C_1\,L_2^2\,n} < 0$$

$$I_{TH} < \frac{V_s \, t_q \left(6 \, C_1 \, L_2 - t_q^2\right)}{6 \, C_1 \, L_2^2 \, n} \qquad \text{Eq. 35}$$

In this design, voltage source is rated at 28 V and the threshold current is 5 A.

$$\begin{cases} V_s = 28\text{V} \\ I_{TH} = 5 \text{ A} \end{cases}$$

Normally, t_q is around 20 μs. If the turn ration and the capacitance values are fixed at 3 and 50 μF respectively, L_1, L_2 and L_M can be obtained using the expression 35, turn ratio and the mutual inductance equation:

$$L_2 = 1{,}33 \text{ μH} \rightarrow L_2 = 1{,}5 \text{ μH}$$

$$L_1 = n^2 \, L_2 = 13{,}5 \text{ μH} \qquad \text{Eq. 36}$$

$$L_M = k\sqrt{L_1 L_2} = 4{,}455 \text{ μH} \qquad \text{Eq. 37}$$

Where k is the coupling factor and it has a value of 0,99.

Circuit parameters are written in the following table:

Table 16   SSCB parameters

Parameter	Value
V_s	28 V
I_{TH}	5 A
t_q	20 μs
L_1	1,5 μH
L_2	13,5 μH
L_M	4,455 μH
$C_{1,2}$	50 μF
$R_{1,2}$	50 Ω

R_1 and R_2 together with C_1 and C_2 respectively will determine the charging time of capacitors (regardless of the diode voltage drop). Capacitor charging process in the circuit can be seen in figure 38. Assuming the capacitor voltage responds like a first order system, to reach 95 % of the final value, time must be three times the electrical constant τ (figure 39).
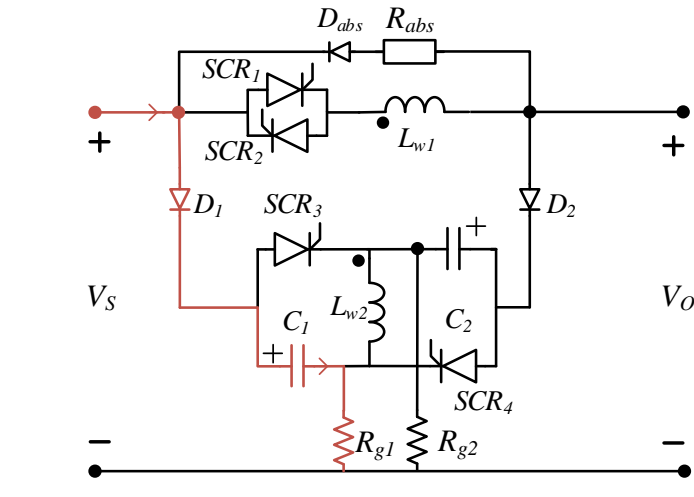

Fig. 38   DC SSCB capacitor charging process

$$t_{95\,\%} = 3\tau = 3RC = 7{,}5 \text{ ms}$$ Eq. 38
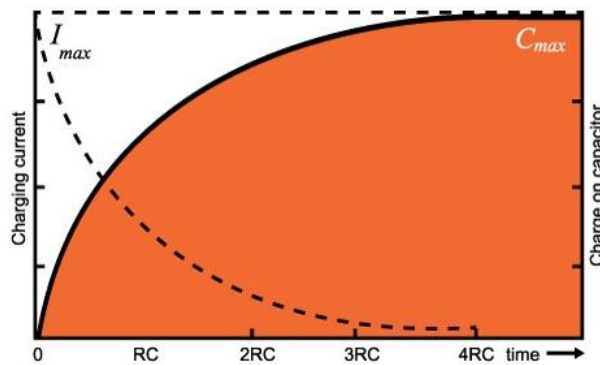

Fig. 39   Capacitor charging process
Source: [15]

6.1.4.   Circuit simulation

Simulink has been used to simulate the circuit. It is composed by a 28 VDC voltage source, the solid-state circuit breaker (grey box), a switch to cause a short circuit between positive and negative terminals and a 10 Ω load (see figure 40). The step time for this simulation is 10 ns. As explained before, when current through the load overcomes the threshold current (5 A),

contactor will generate a pulse signal to activate the SCR3, allowing C1 to discharge into the second coil of the coupled inductor. Then, an induced current opposing the fault current sense will be induced and it will deactivate SCR1 denying the current flow through the load.
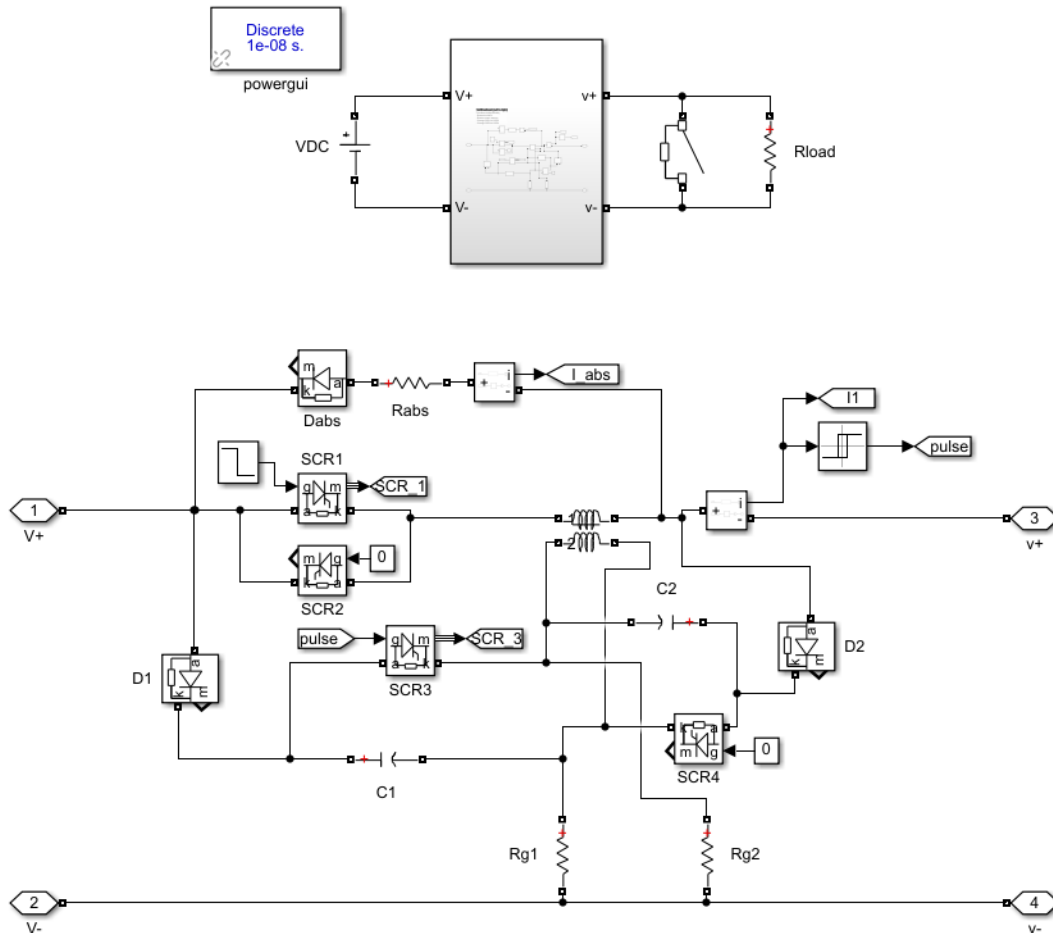

Fig. 40   DC SSCB block system

Figure 41 shows generator voltage, primary inductor current, load voltage and load current respectively. Once the short circuit occurs, primary inductor current starts increasing until the threshold current (5 A). At this point, primary inductor current experiences a fast decrease due to SCR1 switching off and the fault is now isolated. Both load voltage and current drop just at the start of the fault while generator voltage remains constant during all this process. Increasing and decreasing primary inductor current ramp last for 1,02 μs and 32,63 ns respectively.
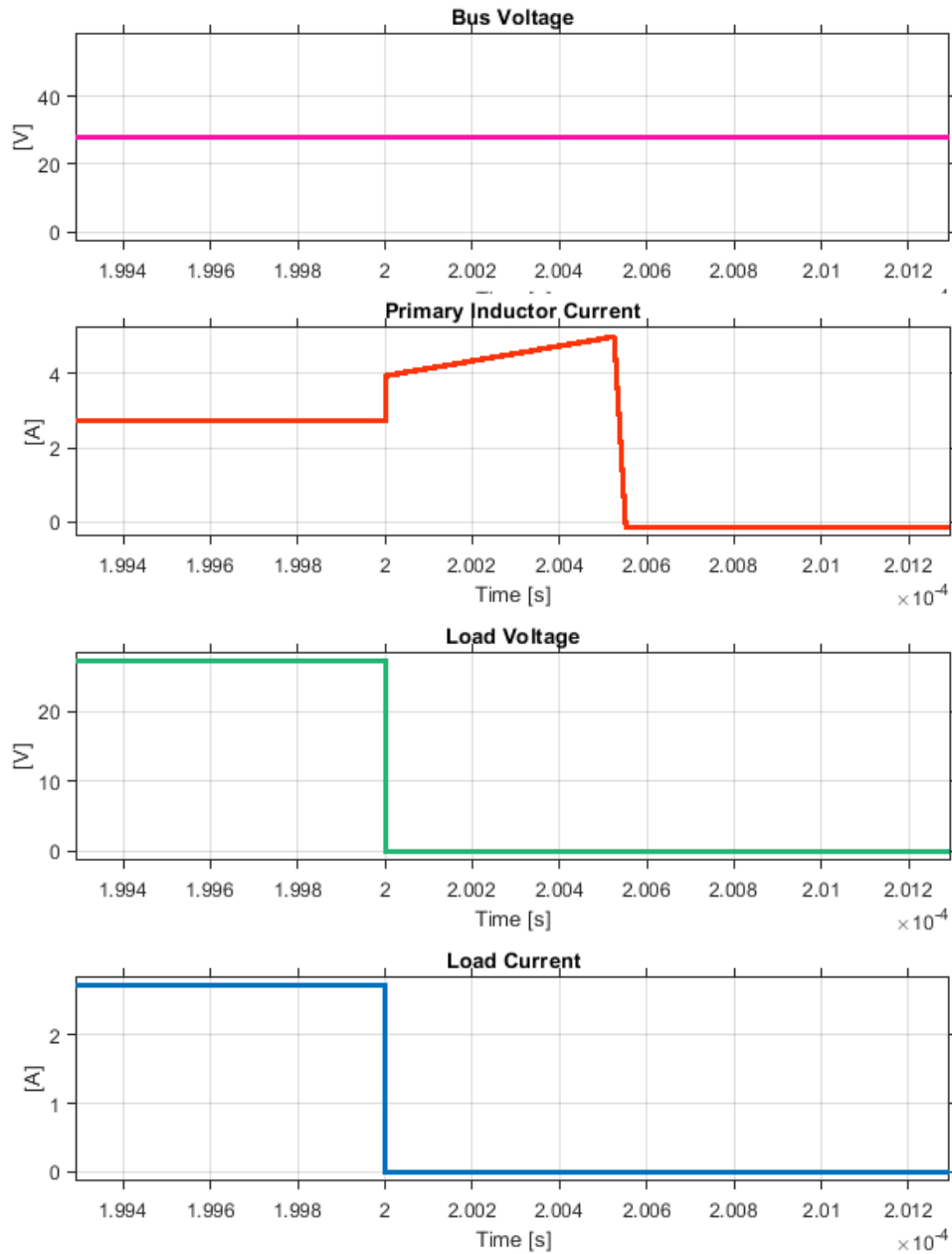
Fig. 41   DC SSCB waveforms

Figure 42 shows, in this order, load current, SCR1 current or primary inductor current, SCR3 current and absorption current. It can be seen, SCR3 only needs a short current pulse (26,84 µs) to activate it. On the other hand, last diagram reveals the absorption current waveform which is a decreasing current ramp as expected.
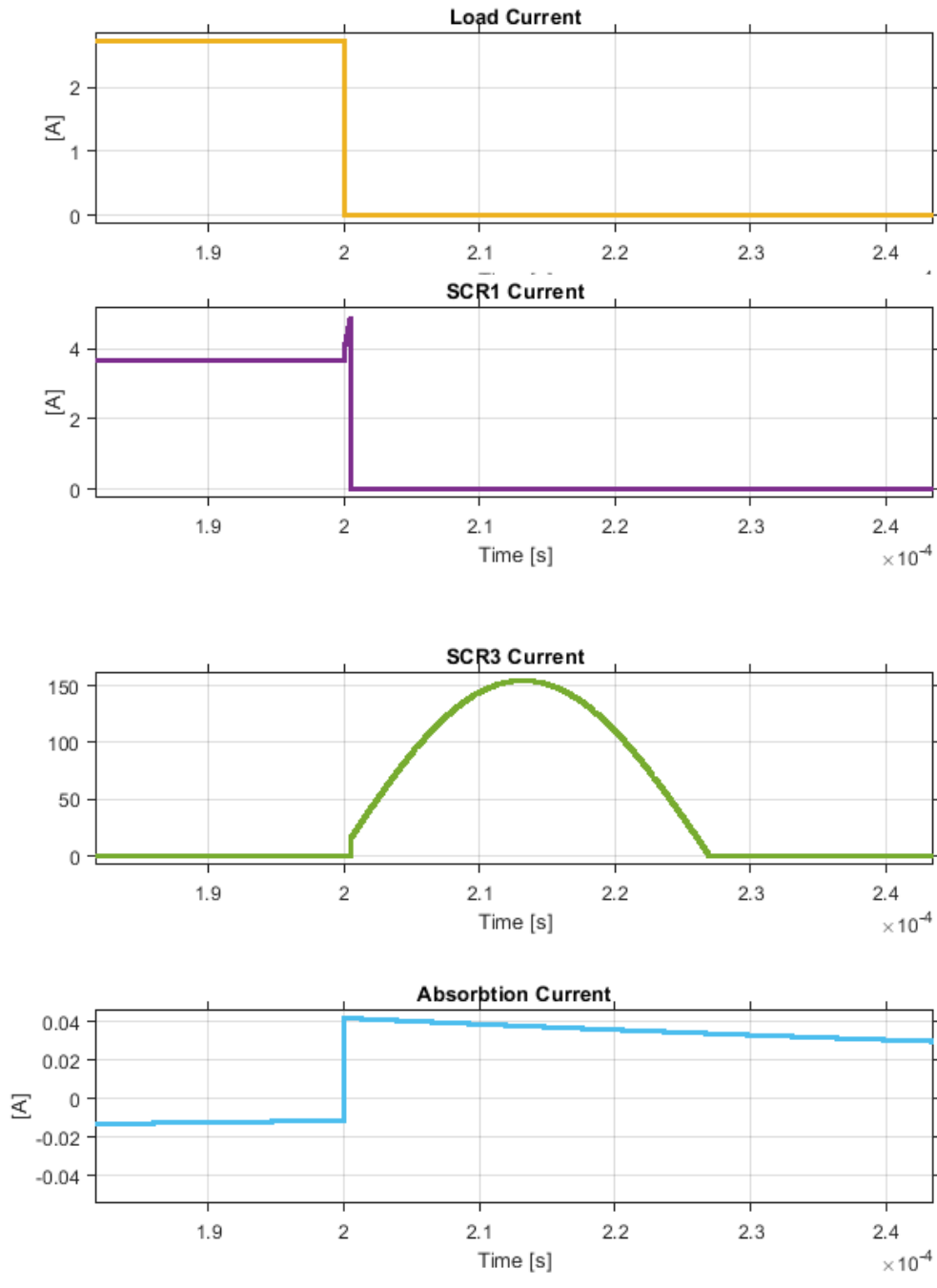
Fig. 42   DC SSCB waveforms

The below figure 43 presents the charging and discharging process of the capacitor. It can be seen the charging step again after the fast discharge when the fault occurs. The theoretical time to reach 95 % of the final value is 7,5 ms. In the simulation, at 7,5 ms, instantaneous voltage value is 25,85 V which represents 92,32 % of the final value (28 V).
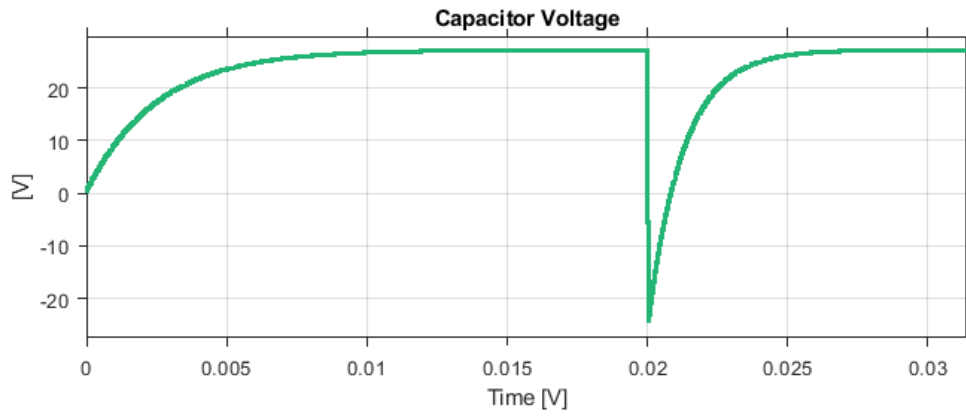
ETSEIB

Fig. 43   Capacitor charging and discharging waveforms

Figure 44 is a closer look to figure 43. It shows the discharging current pulse clearly and it lasts around 27 µs.
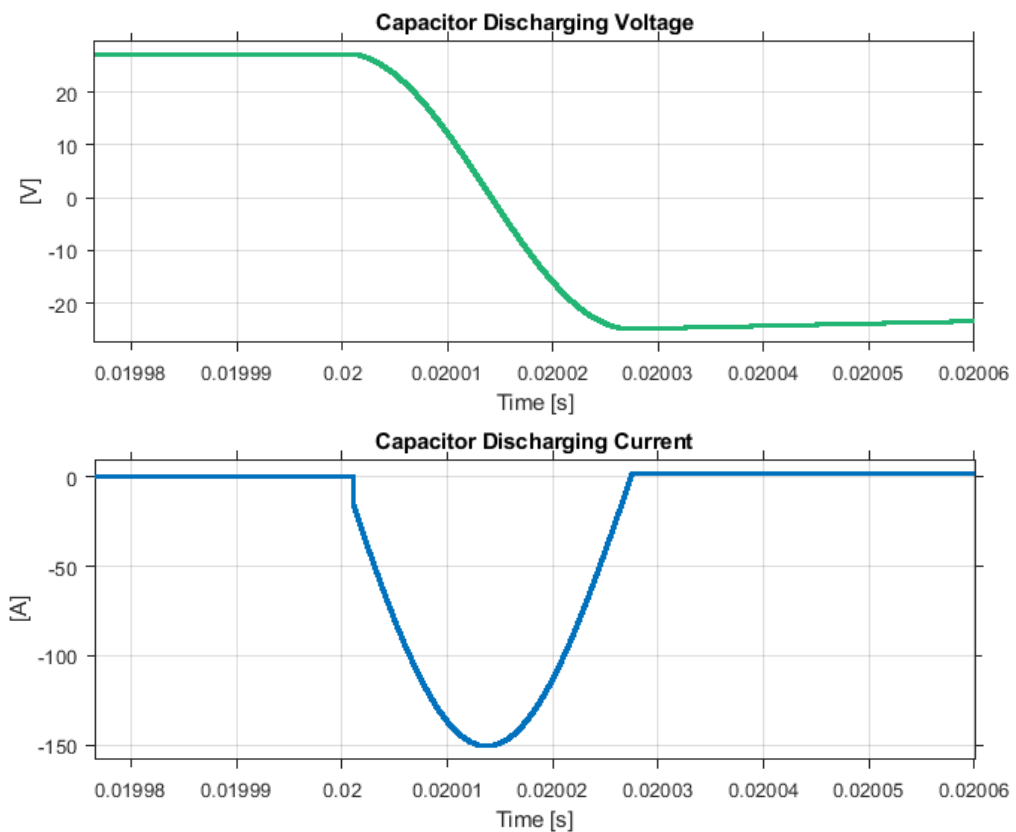

Fig. 44   Capacitor discharging waveforms

6.2. AC overcurrent protection

AC overcurrent protection is based on a circuit breaker that opens the circuit either if RMS or peak current value exceeds the limit. Every phase is checked and a boolean signal is sent through the output terminal after the AND gate. There is a timer that keeps the switch closed for 0,01 s at the beginning of the simulation to avoid opening the circuit while RMS value is not yet calculated. Figure 46 shows the checking system inside the circuit breaker control block from figure 45.

As seen in figure 45, two programable switches are connected between two load phases and one phase to ground to cause a short-circuit. Current measurement blocks are placed to trigger the main circuit breaker.
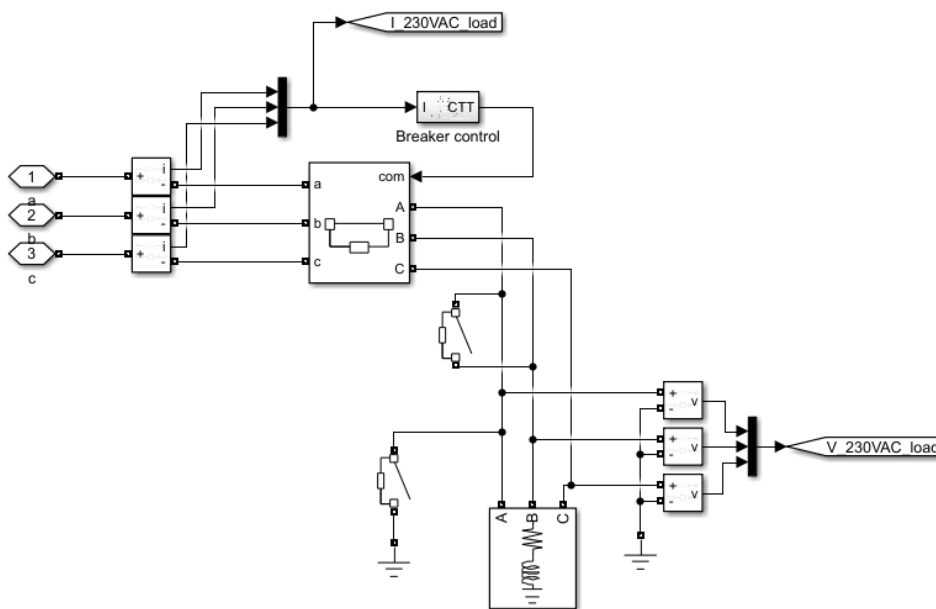

Fig. 45   AC circuit breaker block system
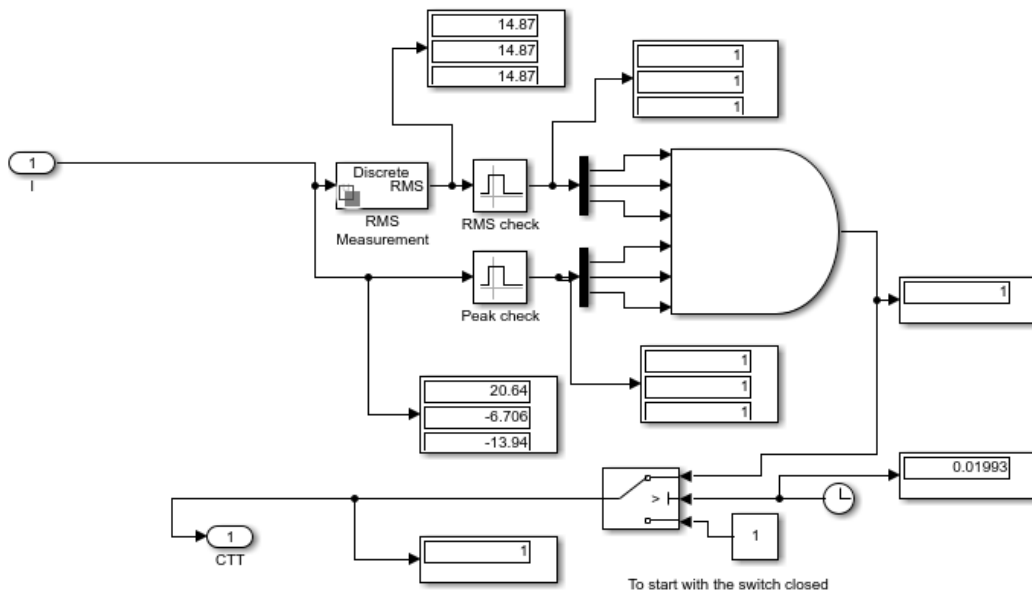
Fig. 46   Circuit breaker control block system

6.3. Simulation study of fault tests

6.3.1. Phase-to-phase short-circuit on the DC load

Figure 47 shows loads one and two connected in parallel to the 28 VDC bus. There is a switch to short-circuit positive and negative terminals of the bus upstream load 2 (10 Ω). The SSCB only protects load 2 since it is placed before this one.
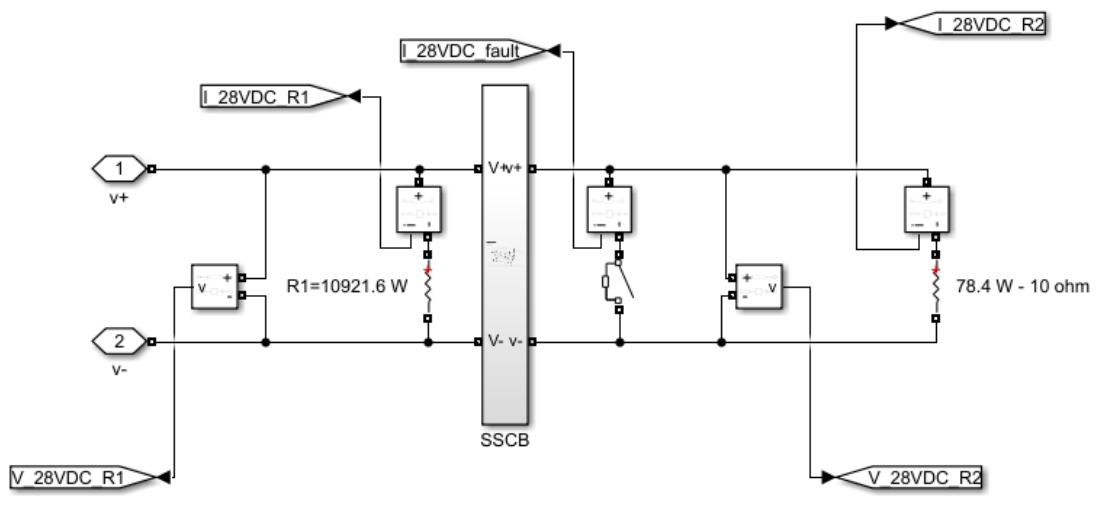

Fig. 47   DC loads and SSCB block system

As seen in figure 48, during the fault, load 1 waveforms remain the same because the short-circuit only affects load 2. However, in the second load, the fault is extinguished and isolated instantaneously.
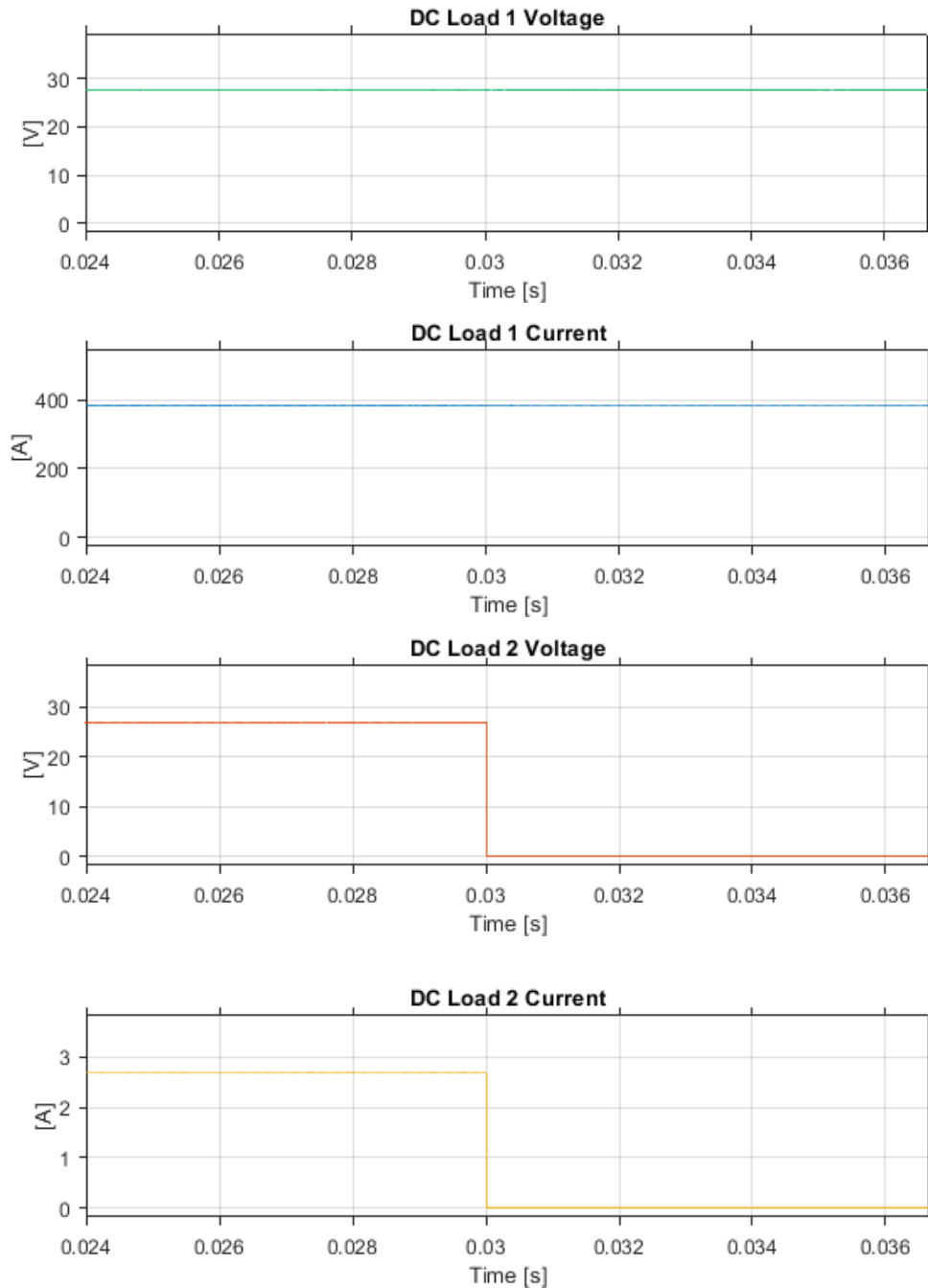
Fig. 48   DC short-circuit waveforms

6.3.2. Phase-to-phase short-circuit in the variable frequency load

When there is a short-circuit between terminals of the variable frequency load, it does not only affect the variable frequency bus but also the DC bus (figure 49). This is because the variable frequency bus powers the DC bus and the rectifier is uncontrolled. It does not affect the constant frequency bus since it uses a controlled inverter.
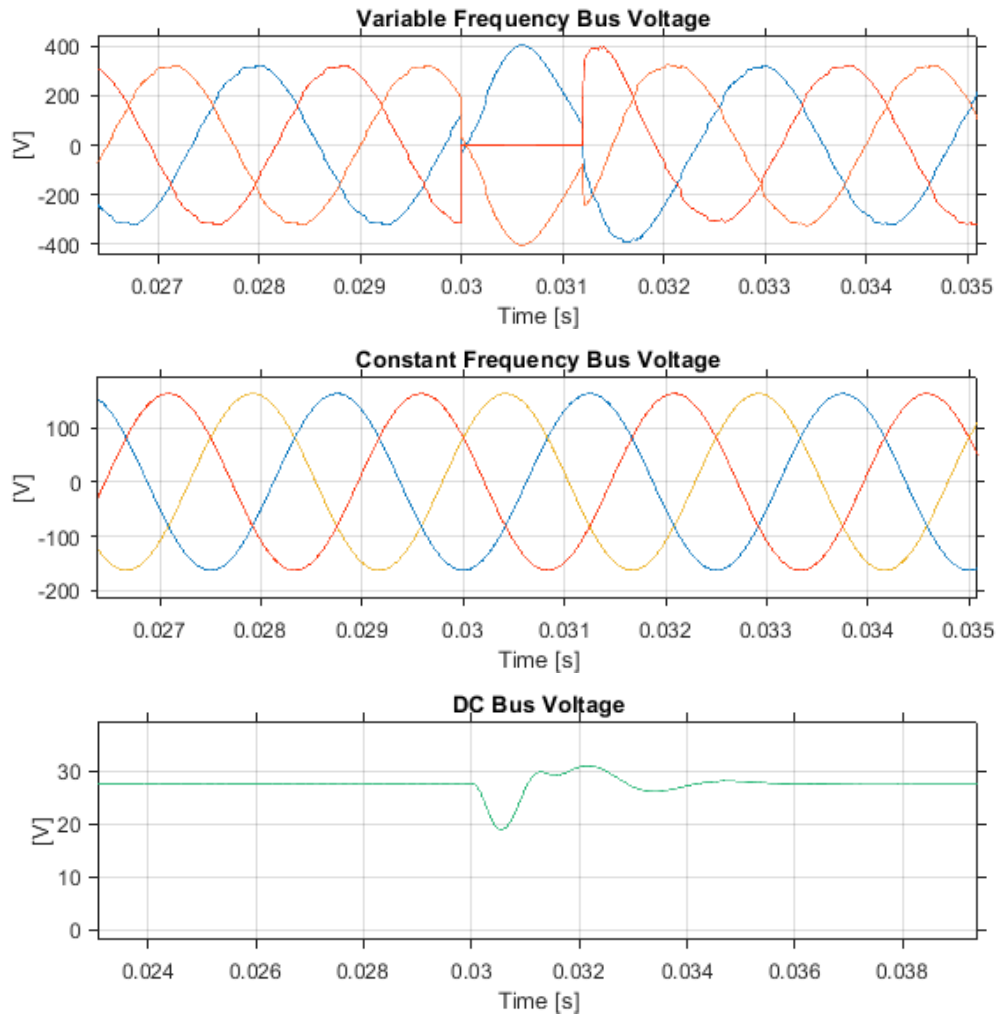
Fig. 49   Bus waveforms during a phase-to-phase AC short-circuit

Figure 50 shows the fault isolation process between load terminals. The AC circuit breaker takes 1,263 ms to isolate the fault.

Fig. 50   Load terminals during a phase-to-phase AC short-circuit

6.3.3.   Phase-to-ground short-circuit in the variable frequency load

As shown in figure 51, a Phase-to-ground short-circuit in the variable frequency load also influences the DC bus and it isolates the fault in 1,089 ms.

Fig. 51   Load terminals during a phase-to-ground AC short-circuit

7. Environmental impact

To start this chapter, it could be interesting to review a few facts as regards aviation emissions [4]. In 2019, flights produced 915 million tonnes of CO_2 worl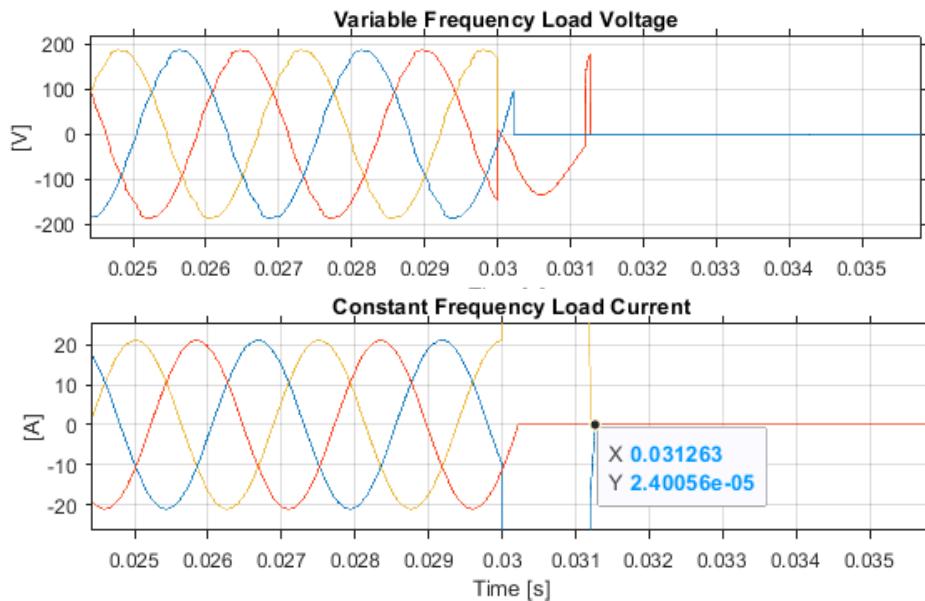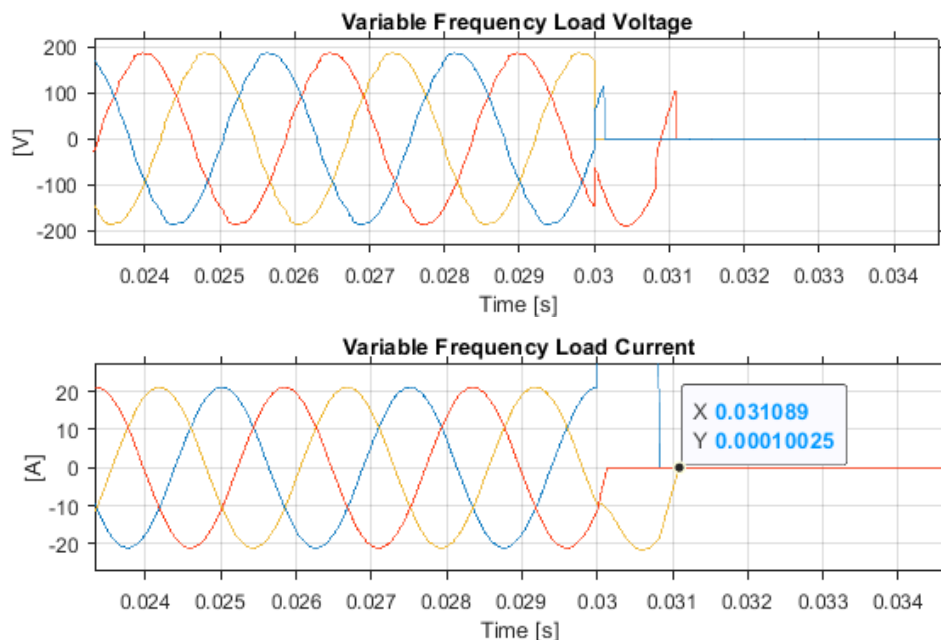dwide. The magnitude of the problem can be understood if this number is compared to the global human CO_2 production (43 billion tonnes of CO_2). It represents 2,1 % of all human carbon dioxide emissions.

If transport sources are analysed, aviation is responsible for 12 % of CO_2 emissions from all transport sources while road transport represents the 74 %. Inside aviation, narrow body aircraft such as Boeing 737, and wide body aircraft, such as Boeing 787 and Airbus 380, are responsible for about 43 % and 33 % of aviation greenhouse gas emissions respectively [23].

On the other hand, it has to be said that around 80 % of aviation CO_2 emissions are from flights for which there is no practical alternative transport mode, i.e., flights over 1500 kilometres. Furthermore, aviation is an efficient transport system in terms of occupancy. Globally, the average aircraft occupancy is almost 83 %.

There are four main high-priority approaches regarding Carbon Dioxide emissions reduction [13]. These are listed below:

• Advances in aircraft–propulsion integration

• Improvements in gas turbine engines

• Development of turboelectric propulsion systems

• Advances in sustainable alternative jet fuels

Finally, the Advisory Council for Aviation Research and Innovation in Europe proposed a few ambitious climate targets in 2018 for a short-term task (2020) and a long-term task (2050) [20].

Table 17   Climate targets for 2020 and 2050
                  Source: [20]

Goals	Vision 2020	Vision 2050
CO_2 emission reduction	50%	75%
NO_x emission reduction	80%	90%
External noise reduction	50%	65%
Fuel consumption reduction	50%	—

They not only consider targets about CO_2 emissions, but they also contemplate other aspects such as NO_X emissions, external noise and fuel consumption. The council hope global civil aviation operations will achieve a further 25 % reduction in CO_2 emissions and a 10 % reduction in NO_X emissions by 2050.

Conclusions

A More Electric Aircraft microgrid has been designed and simulated successfully with the purpose of improving some of its electrical constants. This simulation can be a useful tool to check if a certain converter topology would suit an aircraft microgrid, to evaluate whether a protection would work or not, or to analyse the most efficient power distribution system before building any prototype. It is essential to simulate first the interactions between elements of such microgrids because each of these components can be very expensive.

The results have shown that essential parameters meet the standards required by DO160-G under normal operation. It has been demonstrated that the system can extinguish and isolate different faults in more than acceptable times. Despite DC SSCB are often complex, they can be more reliable and efficient than traditional AC ones mainly due to the use of power electronics.

After the literature review, it can be concluded that the most promising power distribution architecture is DC topology since it is the lightest and the most efficient one. That is why the top aircraft research groups such as MOET EU, CleanSky project and Airbus HVDC project are studying this distribution topology.

Regarding future actions, it would be interesting to replace passive rectifiers with controlled rectifiers. It would help improving the system efficiency, but a more sophisticated control strategy would be necessary. Finally, it would be engaging to simulate a DC power distribution since it seems that future aircraft will be based on this topology.

ETSEIB

Acknowledgements

I want to thank my family and friends for all the encouragement they have given me over the years. Especially to my parents, Josep and Concep for all their unconditional support throughout my life.

I would also like to thank Sheng Wang, Wenlong Ming and Yufeng Yang for supervising and helping me with the project at Cardiff University.

ETSEIB

Bibliography

Bibliographical references

[1] K. Xu, N. Xie, C. Wang and Y. Wang, "A comprehensive simulation model and stability analysis for power system of more electrical aircraft," *2016 IEEE International Conference on Aircraft Utility Systems (AUS)*, 2016, pp. 219-226, doi: 10.1109/AUS.2016.7748050.

[2] XU, Kelu, et al. Modeling and simulation of variable speed variable frequency electrical power system in more electric aircraft. *The Open Electrical & Electronic Engineering Journal*, 2017, vol. 11, no 1.

[3] Mohan, N., Undeland, T. and Robbins, W. (1995). *Power Electronics.* 2nd ed. John Wiley & Sons, Inc, p.468-470.

[4] "Facts & figures", *Air Transport Action Group*, 2022. [Online]. Available: https://www.atag.org/facts-figures.html. [Accessed: 02- Sep- 2022].

[5] Y.-S. Lee and M. H. L. Chow, "Three phase bridge rectifier," *Three Phase Bridge Rectifier - an overview | ScienceDirect Topics*. [Online]. Available: https://www.sciencedirect.com/topics/engineering/three-phase-bridge-rectifier. [Accessed: 23-Mar-2022].

[6] Dursun, Mustafa & Dosoglu, M.. (2018). LCL Filter Design for Grid Connected Three-Phase Inverter. 1-4. 10.1109/ISMSIT.2018.8567054.

[7] D. Collins, "FAQ: What is a pulse rectifier and what kinds are there?", *Motioncontroltips.com*, 2022. [Online]. Available: https://www.motioncontroltips.com/faq-what-is-a-pulse-rectifier-and-what-kinds-are-there/. [Accessed: 02- Sep- 2022].

[8] Yagnik, Utsav & Solanki, Mehul. (2017). Comparison of L, LC & LCL filter for grid connected converter. 455-458. 10.1109/ICOEI.2017.8300968.]

[9] X. Xu et al., "A Novel Thyristor-Based Bidirectional SSCB With Controllable Current Breaking Capability," in IEEE Transactions on Power Electronics, vol. 37, no. 4, pp. 4526-4534, April 2022, doi: 10.1109/TPEL.2021.3122583.

[10] Y. Wang, R. Dong, Z. Xu, Z. Kang, W. Yao and W. Li, "A Coupled-Inductor-Based Bidirectional Circuit Breaker for DC Microgrid," in IEEE Journal of Emerging and Selected Topics in Power Electronics, vol. 9, no. 3, pp. 2489-2499, June 2021, doi: 10.1109/JESTPE.2020.3016647

[11] A. Sguarezi Filho, "Induction machine and three-phase power converter dynamic models", 2022. [Online]. Available: 11. https://www.sciencedirect.com/topics/engineering/sinusoidal-pulse-width-modulation. [Accessed: 02- Sep- 2022].

[12] Andrada, P. (n.d.). *Apunts de Disseny de Màquines i Accionaments Elèctrics.* Barcelona: Departament elèctric ETSEIB, Chapter 3 page 25.

[13] National Academies of Sciences, Engineering, and Medicine 2016. *Commercial Aircraft Propulsion and Energy Systems Research: Reducing Global Carbon Emissions.* Washington, DC: The National Academies Press, p. 88-89. https://doi.org/10.17226/23490

[14] Haitham Abu-Rub; Mariusz Malinowski; Kamal Al-Haddad, "Power Electronics for More Electric Aircraft," in *Power Electronics for Renewable Energy Systems, Transportation and Industrial Applications* , IEEE, 2014, pp.365-386, doi: 10.1002/9781118755525.ch12.

[15] "Capacitor Charge and Time Constant Calculator", *Allaboutcircuits.com*, 2022. [Online]. Available: https://www.allaboutcircuits.com/uploads/articles/Capacitor-Charge-and-Time-Constant-Calculator.jpg. [Accessed: 02- Sep- 2022].

[16] L. Dorn-Gomba, J. Ramoul, J. Reimers and A. Emadi, "Power Electronic Converters in Electric Aircraft: Current Status, Challenges, and Emerging Technologies," in IEEE

Transactions on Transportation Electrification, vol. 6, no. 4, pp. 1648-1664, Dec. 2020, doi: 10.1109/TTE.2020.3006045.

[17] B. Rahrovi and M. Ehsani, "A Review of the More Electric Aircraft Power Electronics," 2019 IEEE Texas Power and Energy Conference (TPEC), 2019, pp. 1-6, doi: 10.1109/TPEC.2019.8662158.

[18] Rosero, J.A., Ortega, J.A., Aldabas, E., and Romeral, L. (2007) Moving Towards a More Electric Aircraft. IEEE A&E Systems Magazine, pp. 3–9

[19] Moir, I. and Seabridge, A. (2008) *Aircraft Systems: Mechanical, Electrical and Avionics Subsystems Integration*, 3rd edn, John Wiley & Sons, Ltd.

[20] J. Chen, C. Wang and J. Chen, "Investigation on the Selection of Electric Power System Architecture for Future More Electric Aircraft," in IEEE Transactions on Transportation Electrification, vol. 4, no. 2, pp. 563-576, June 2018, doi: 10.1109/TTE.2018.2792332.

[21] B. H. Nya, J. Brombach and D. Schulz, "Benefits of higher voltage levels in aircraft electrical power systems," *2012 Electrical Systems for Aircraft, Railway and Ship Propulsion*, 2012, pp. 1-5, doi: 10.1109/ESARS.2012.6387381.

[22] V. Madonna, P. Giangrande and M. Galea, "Electrical Power Generation in Aircraft: Review, Challenges, and Opportunities," in *IEEE Transactions on Transportation Electrification*, vol. 4, no. 3, pp. 646-659, Sept. 2018, doi: 10.1109/TTE.2018.2834142.

[23] A. Barzkar and M. Ghassemi, "Electric Power Systems in More and All Electric Aircraft: A Review," in IEEE Access, vol. 8, pp. 169314-169332, 2020, doi: 10.1109/ACCESS.2020.302416